DEPTH ASSESSMENT OF AN ABSORBER IN A SEMI-INFINITE MEDIUM BY CONTINUOUS WAVE DIFFUSE REFLECTANCE

by

Ertuğrul Burteçin Aksel

B.S, Engineering in Physics, Technical University of Istanbul, 1995

M.S, Institute of Biomedical Engineering, Boğaziçi University, 2001

Submitted to the Institute of Biomedical Engineering

in partial fulfillment of the requirements

for the degree of

Doctor

of

Philosophy

Boğaziçi University

2018

ACKNOWLEDGMENTS

I would like to express my deepest thanks to all the members of the jury, my thesis advisor Prof. Dr. Murat Gülsoy, and thesis co-advisor Prof. Dr. Ata Akın , Prof. Dr. Yekta Ülgen , Prof. Dr. Can Yücesoy, Prof. Dr. Ahmet Ademoğlu and Assistant Prof. Dr. Burcu Tunç for their thorough comments and valuable amendments for the being of my thesis.

The complication of this work would have never ended without the peerless mentorship of my thesis advisor Prof. Dr. Murat Gülsoy.

And very singular thanks to Prof. Dr. Ata Akın, who, during the process of this work, provided me with all necessary hardware, software, manpower and experimental setup as well as his inspiring and treasured academic contribution and comments. Without his presence, this thesis would have never been existed.

During the progress of the thesis, Ece Ercan and Ahu Nur Türkoğlu played a very crucial role to have conducted the experiments in a very thorough and neat way. It was a great chance for me to have found such devoted and enthusiastic experimenters as them.

Through all my years of assistantship and education in the Institute of Biomedical Engineering, Boğaziçi Üniversitesi, I have to exclusively mention devotedness and consideration of the directors of the Institute, Prof. Dr. Yorgo İstefanopulos, Prof. Dr. Yekta Ülgen. Without their administration, this thesis would have never been completed. I, also, must mention, my MSc thesis advisor Prof. Dr. Mehmed Özkan for his valuable contribution to my academic background. I must mention the friendship and intimacy of Prof. Dr. Ahmet Ademoğlu as well as his unique academic contribution to my academic development through my years in the institute.

Bora Büyüksaraç, my colleague and only office mate has always been the first person to have discussed academic and daily life issues. Asım Samlı, Tuna Aydın, Dilek Göksel-Duru, Özgür Tabakoğlu, Özgüncem Bozkulak, Gökhan Işık, Alper Yaman and Didar Talat were all valuable for their friendship. Erhan Uyanık, reserves very special thanks for his friendship. Özgür Kaya, with his great expertise on Latex,has eased my troubles with the editing of the thesis. I owe many thanks to him. I, here, have to mention Kaan Öztürk and Aslı Umur for their matchless friendship.

Even though, it is impossible to express my true gratitude to him, grand Mustafa Kemal Atatürk, my most sincere and true thanks are to him. "Hayatta en hakiki mürşit ilimdir,fendir."

And many thanks to my family my beloved mother Güneşhan, my beloved father Ekrem and my sister Selcen.

And my "biriciklerim", my beloved wife Ayla, and my son Güneş Tardu: Your presence and value cannot be described with any word, so I do not even dare to start to make a description of value of Your presence for me.

ACADEMIC ETHICS AND INTEGRITY STATEMENT

I,Ertuğrul Burteçin Aksel, hereby certify that I am aware of the Academic Ethics and Integrity Policy issued by the Council of Higher Education (YÖK) and I fully acknowledge all the consequences due to its violation by plagiarism or any other way.

Name : Signature:

_____ _____

Date:

_____

ABSTRACT

DEPTH ASSESSMENT OF AN ABSORBER IN A SEMI-INFINITE MEDIUM BY CONTINUOUS WAVE DIFFUSE REFLECTANCE

A method to locate an absorber embedded in a semi-infinite turbid medium by spatially-resolved continuous-wave diffuse reflectance measurements is introduced. The possible of use the method as a priori information in diffuse optical imaging is discussed. The depth of the absorber is assessed by single wavelength spatially-resolved continuous-wave diffuse reflectance measurements by two detectors in a radial row. The ratio of perturbations introduced by the defect at two detectors is used to be matched with Ratio-vs.-Depth curve which are generated by approximate formulae of continuous wave diffuse reflectance. The error due to approximation and the error in depth assessment are studied for different cases revealing favorable source-detector placements with respect to planar position of the defect. The effect of lateral displacement of the source with respect to defect is studied. A strategy to overcome errors introduced by erroneous prediction of background medium optical properties is suggested. Theoretical results indicate that the depth of the absorber can be obtained with 0.1 mm precision independent of its absorption coefficient and its size for the values chosen in the study. The approach is tested experimentally, and it is observed that theoretical results fit with experimental data.

Keywords: Spatially-resolved continuous wave diffuse reflectance, absorber localization, a priori information, diffuse optical imaging.

ÖZET

SAÇKAN YARI-SONSUZ ORTAMDA BİR SOĞURGANIN UZAMSAL-AYRIŞMIŞ SÜREKLİ-DALGA YAYIK YANSIMA ÖLÇÜMLERİYLE KONUMLANDIRMASI

Yarı-sonsuz saçkan bir ortama gömülü bir soğurganın konumlandırımlası için uzamsal-ayrışmış sürekli-dalga yayık yansıma ölçümlerine dayanan bir metod önerilmiştir. Soğurganın derinliği tek dalga boyunda uzamsal-ayrışmış yayık yansımanın tek çizgi üzerinde bulunan iki algıç tarafından ölçülmesiyle kotarılır. Soğurganın algıçlardaki ölçümde yol açtığı kaymaların oranı ile sürekli dalga yayık yansıma denklemleri ile bulunan Orana-karşı-Derinlik Eğrileri karşılaştırılması ile soğurganın derinliği bulunur. Formülasyondaki yaklaşıklığın yol açtığı ve derinlik kestirimindeki hatalar değişik kaynak-algıç yerleştirilmeleri için çalışılmıştır. Kaynağın soğurgana göre yanyönklü yerleştirilmesinin etkisi çalışıldı. Arkaortamın optic özelliklerinin yanlış öngürüsü dolayısıyla meydana gelebilecek hatalar için de bir strateji önerilmiştir. Çalışmanın teorik bulguları bir soğurganın derinliğinin 0.1 mm kesinlik ile soğurganın soğurma katsayısı ve ebatından bağımsız olarak elde edilebildiğini göstermiştir. Yaklaşım deneylerle sınanmış ve teorik sonuçların deneyle uyuştuğu görülmüştür.

Anahtar Sözcükler: Uzamsal-ayrışmış sürekli dalga yayık yansıması, soğurgan konumlandırılması, yayık optic görüntüleme.

TABLE OF CONTENTS

LIST OF FIGURES

LIST OF TABLES

LIST OF SYMBOLS

g	Anisotropy constant of scattering [-]
$\sigma_a(\lambda)$	Absorption cross-section as function of illumination wavelength [L^2]
$\sigma_s(\lambda)$	Scattering cross-section as function of illumination wavelength [L^2]
$\rho_a(\vec{r})$	Local concentration of absorbers inside medium [L^{-3}]
$\rho_s(\vec{r})$	Local concentration of scattering inside medium [L^{-3}]
$\mu_a(\vec{r}, \lambda)$	Linear absorption coeffient inside medium [L^{-1}]
$\mu_s(\vec{r}, \lambda)$	Linear scattering coeffient inside medium [L^{-1}]

LIST OF ABBREVIATIONS

ATP	Adenosine triphosphate
CW	Continuous Wave
DOI	Diffuse Optical Imaging
DOT	Diffuse Optical Tomography
fNIRS	functional Near-infrared Spectroscopy
EM	Electro-magnetic
FD	Freqeuncy Domain
HbR	De-oxy Hemoglobin
HbO_2	Oxy Hemoglobin
HG	Henyey-Greenstein
J_0	Response of the homogeneous medium
J_1	Perturbation in the measurement due to the defect
J_T	Total flux density
NIR	Near Infrared
OCT	Optical Coherence Tomography
PMIS	Photon-Material Interaction Site
RG	Rayleigh-Gans
RTE	Radiative Transfer Equation
SRCW	Spatially resolved continuous wave
SC_x	Source-to-the-center-of-defect Distance
SPD	Source-Proximal Detector
SPF	Scattering phase function
SSP	Shaped Spatial Sensitivity
TD	Time Domain

1. INTRODUCTION

Use of optical radiation of visible and near-infrared (NIR) range in medicine for diagnosis and treatment has been attractive due to its non-hazardous character with respect to radiation in other ranges (X-ray, gamma). In 1929 Cutler [1], a method based on visual inspection of trans-illuminated visible light transillumating human breast was proposed and had been implemented till 1970's and early 1980 [2]. This method has been abandoned after a multi-center study has exposed its weaknesses with respect to conventional mammography [2]. On the other hand, it was shown by Jobsis that [3] it is possible to monitor oxygenation state of a cat's brain in vivo non invasively by measuring changes in intensity of NIR light passing across the head of the cat. Subsequently a great amount of work dedicated on the improvement of understanding light-tissue interaction, modeling of NIR and visible photon migration in highly-scattering media and more fruitful use of NIR light in medicine has appeared in last 4 decades.

A significant but "evolutionary but not revolutionary" [3] [4] progress is seen in biomedical optics using NIR and visible light resulting in different modalities like diffuse optical tomography (DOT), functional near-infrared spectroscopy (fNIRS). Even though they are given different names, there is a common point among these: they all depend on collecting diffusely reflected or transmitted light by optical detectors which is injected into the medium by optical sources. In the evolution of the field, mostly three different approaches for collecting data are used: continuous-wave (CW), frequency-domain (FD) and time-domain (TD).

An optical in-homogeneity in turbid media (e.g. soft tissue) may imply the existence of a hemorrhage, tumor or high saturation of oxygenation in a case where absorption and/or scattering characteristics of tissue changes with respect to the concentration of the natural chromophore. For detection and localization of such optical in-homogeneities, illumination with non-ionizing electro-magnetic (EM) radiation in

NIR or visible region has been utilized. Specifically EM radiation (600-1000 nm) is weakly absorbed inside the biological tissue by experiencing many scattering events per unit length diminishing the availability of ballistic photons [5], [6].

NIR radiation is used in diffuse optical imaging (DOI) or tomography (DOT), which is a medical imaging modality to obtain optical parametric maps of living tissue [7, 8]. The main idea in DOT is the reconstruction of the probed volume by solving a forward model of photon propagation iteratively [4] [7] [9] and to map spatially resolved spectroscopic chromophore concentrations [10–13]. Even though DOT has great advantages, namely use of safe wavelengths, repetitive use, portability and low cost, it suffers from low spatial resolution with respect to other imaging modalities such as X-Ray tomography, magnetic resonance imaging (MRI) and ultra-sound (US) imaging [14–16].

Recently, it has been proposed that the location of a defect inside a turbid medium obtained by a direct localization method could be used as a priori spatial information for recursive algorithms in DOT [17, 18]. Direct localization schemes generally depend on trans-illumination measurements, which can be used for slab, finite-size [4] [17] [19–23] or circular geometries [18]. In contrast, for diffuse reflectance measurements, only a few schemes were proposed to improve the accuracy in localization [24–26]. Time domain (TD) [25,26] and frequency domain (FD) measurements [24] which are complicated with respect to CW measurements [14] have attempted to address this issue but no method exists for the fastest and inexpensive approach that uses the CW illumination.

Knowledge on the depth of an absorber could be incorporated in the process of selecting optimal regularization parameters in both CW and frequency-domain DOI [27,28]. Adapting the modulation frequency in accordance to the known depth coordinates allows increased specificity and sensitivity in DOI [29] and increase in image resolution [30–33]. Under-determinacy of the DOI could also be reduced by introduction of an adaptive grid mesh in the reconstructed volume of interest [33,34]. However, co-registration of images from different modalities has subtleness [34, 35] and different

imaging modalities assess the size of the defects (lesions) differently [36] probably due to the inherently different contrast mechanisms in operation [34] [37].

The goal of this study is to recommend a strategy to estimate the depth of an absorber inside a turbid medium. We address the challenge via a single wavelength SRCW diffuse reflectance for semi-infinite geometry and show that under various probe geometries and optical parameters, it is possible to localize the depth of the absorber to within 0.1 mm precision. The accuracy of the method is analyzed for different combinations of optical properties of the absorber and the medium as well as for different spatial placement of the CW source and detectors on the surface of the medium.

2. THEORY

2.1 Optical Properties of Biological Tissue

The living tissue is interrogated by NIR light in fNIRs and DOT applications. Physically, NIR light is multiply scattered by organelles, especially by mitochondria and cell membranes. Since they are ubiquitous in living tissue, a similar description of NIR light propagation can be applied for different types of living tissue. Therefore, understanding physical principles of light propagation in turbid media is essential before presenting the current models on the topic.

2.2 Light Propagation in soft tissue (turbid media)

Electro-magnetic (EM) radiation is a self-generating physical phenomena without the need of a medium to propagate through [38]. On one hand, it is conceived of a wave-like motion with time and space-varying electric and magnetic fields oscillating perpendicularly and has physical attributes like frequency, wave-length, polarization and momentum. Its mathematical derivation is given by Maxwell's (vector) equations; it conveys energy per unit time and per unit area which is given as Poynting's theorem (vector equation) [38,39]. On the other hand, a particle-like scheme is also used for EM radiation. The EM-particles are called as photons whose existence has been reported experimentally [39]. Photons cannot be chopped into halves, or in other words they are the constituents of EM radiation, for which there is no counterpart in wave description. Photons also do not need a physical medium to propagate. Even though the presence of a medium is not necessary for EM propagation, the characteristics of the medium modulate radically the EM radiation [38].

EM radiation in vacuum away from the source (far field radiation) is given by solution of Maxwell's equation where there are no free electric charge and free cur-

rent. Under these circumstances (optically isotropic, non-conducting medium), EM radiation propagates and conveys energy in parallel wave fronts in far field (far from the radiator, qualitatively a distance much bigger than the wavelength of the radiation) which is a function of both time and space Eq. 2.1 and Eq.2.2 [40]. Since there are

$$\vec{E} = \vec{E}_0 e^{(\vec{k}.\vec{r}-wt)} \tag{2.1}$$

$$\left|\vec{B}\right| = \frac{\left|\vec{E}\right|}{c} \tag{2.2}$$

no interaction sites (scatters) for EM in vacuum (which can be considered the only "real" homogeneous medium available), EM does not scatter and continues its propagation theoretically till infinity without a change in its incident direction.

In the case of EM propagation in heterogeneous medium, however, the situation above depicted changes significantly. EM radiation encountering a "heterogeneity" in the course of its propagation, e.g. a molecule, an atom or a particle with a different refractive index with respect to material matrix, oscillates electric charges of the obstacle. As a result of this interaction, accelerated charges radiate secondary radiation, which is named as scattering. The direction and wavelength of the secondary radiation is a complex function of many mechanisms but direction roughly can be thought as a function of the size of the scatterer with respect to the wavelength of the incident radiation [38]. According to Mie's theory [38] [40], as the size of the obstacle is similar or bigger relative to the size of the incident wavelength, re-radiation of the obstacle is biased in forward direction. The superposition of scattered wavelets results in the EM power at a distant point. Since the superposition of wavelets is constructive or destructive at a certain point it is a function of the phase differences among re-radiating dipoles thus phase differences play essential role in determining direction of scattering (Figure 2.1). If a particle is subject to a monochromatic radiation, all dipoles oscillate

in

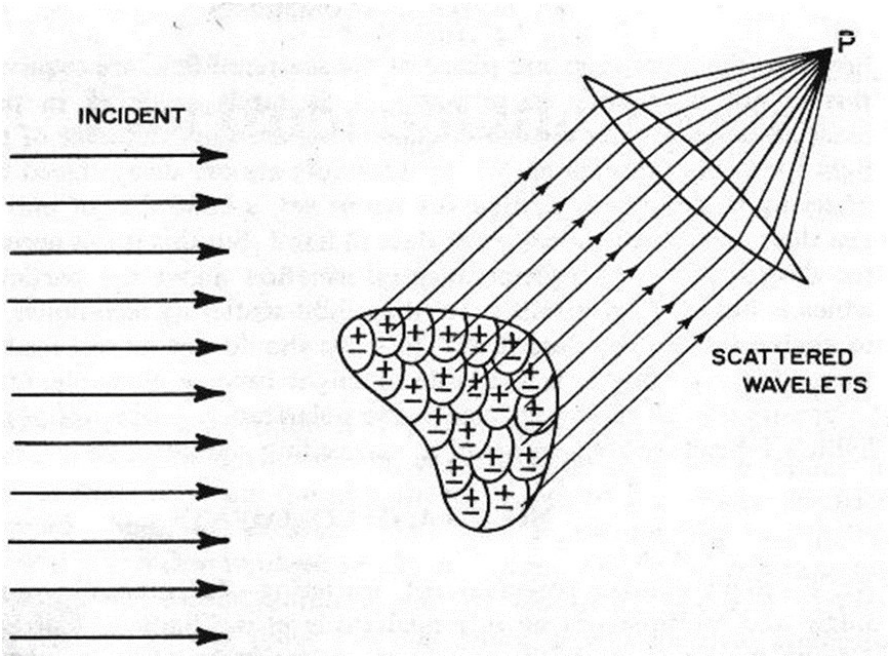

Figure 2.1 A (small) particle (dielectric) is subject to incident radiation from left. Constituents of the particle oscillate as individual dipoles and re-radiate scattered wavelets. At point P scattered wavelets of sources interfere to result in intensity depending on the phase of the source [9] [38].

the same phase. The phase differences of scattering dipoles of the particle that is detected at the point P (Figure 2.1) depend only on their relative position to that point [41]. The size of the particle determines the relative positions of dipoles to point P. Therefore, if the particle is small relative to the wavelength of the incident radiation, re-radiation is isotropic, because all dipoles radiate in phase with respect to any point in space. As the size of the particle is the same or bigger than the wavelength, the phase differences among oscillating dipoles are more pronounced and interfere such that a forward-peaked re-radiation occurs. Mie Theory [38] calculates re-radiation pattern by spheres as a function of radius. Wavelength of re-radiation depends on the internal structure of the particle. The other result of the interaction between EM and the particle is the excitation of the charges present in the particle. In cases where this excitation is transformed into thermal energy, the process is called absorption [38]. Consequently, scattering and absorption are not mutually independent processes.

This qualitative explanation notifies how heterogeneity modifies light propagation embedded in a homogeneous medium, but a careful examination of refrac-

tion/reflection of light at an optically smooth interface signifies another important source of scattering. Most of the media under investigation (including soft tissue) are optically dense; the molecular separation is 2-3 Angstrom ($10^{-10}m$) , which is much smaller than the wavelengths used in NIR (∼700-1000 nm). Under these circumstances, each molecule in a medium exposed to EM radiation is not only influenced by incident light, but also by the resultant of the secondary fields of all other molecules. As it is aforementioned, secondary radiation of a molecule depends on the field to which it is exposed. Thus, this is an electromagnetically many-body case because the molecules are coupled. All these secondary and incident radiations are superposed in a refraction/reflection experiment of light at an optically smooth interface such that the refracted light changes its direction depending on the ratio of refractive indices of media. Meanwhile some portion of the incident light reflects back into the ambient medium in the plane of the incidence. Even though experimental set-up is free from particulate contamination, accurate measurements show that minute amount of light scattered in all directions can be detected which is contradiction to Snell's laws of refraction/reflection [38]. This is due to the fact that medium is statistically homogeneous. In other words, the homogeneity of the medium is distorted by density fluctuations due to thermodynamic arguments. Refractive index of a material can be formulated as follows [41] Eq. 2.3 by a classical treatment,

$$n^2 = 1 + \frac{4\pi N q^2}{M} \frac{1}{{w_0}^2 - w^2} \tag{2.3}$$

where M mass and q is the charge of the resonating molecule, ${w_0}^2$ is natural frequency of the oscillation, w^2 is the driving frequency of the incident light and N is the number of molecules per volume. The fluctuation of molecules of optically dense medium due to thermal agitation results in an in-homogeneity in the density of molecules. This disturbance terminates interference of secondary radiation such that EM radiation in unexpected directions can be detected (in other words scattered radiation). In addition to scattering due to density fluctuations, there are also other types of fluctuations which

cause scattering: concentration fluctuations and orientation fluctuations.

The physical processes taking role in modulating light propagation of arbitrary wavelength in turbid medium are various and complex. However, the picture can be simplified if the medium is statistically homogeneous (atomic and molecular heterogeneity is small compared with the wavelength of the incident light) and the only scatterers assumed are the particles (aggregate of many atoms or molecules) embedded in the medium. Under these circumstances, scattering only due to particles are to be considered because it is much larger than scattering due to fluctuations.

Soft tissue is an aggregation of closely packed groups of cells entrapped in a network of fibers through which water percolates. At a microscopic level, the tissue components have no pronounced boundaries [5]. They appear to merge into a continuous structure with spatial variations in the refractive index. Hence, the propagation of light in soft tissue satisfies the above-mentioned assumptions so that only scattering processes to be considered are the ones by refractive index variations without paying any attention to those by fluctuations. There might be also hard tissue components surrounding the soft tissue (e.g. skull) which does not affect the measurements via NIR related apparatus. A common example is detecting functional brain activation with an fNIRS device. Thus, the presence of a drastically different tissue seems not to be significantly effective in such measurements [42].

2.3 Modeling of light-tissue interaction parameters

Light propagation in soft biological tissue is subject to scattering and absorption. Scattering or absorption of light by the medium per distance is highly probable if absorption and scattering properties of the medium for a wavelength is high. Scattering and absorption can be considered at a microscopic or microscopic level. At the microscopic level, the propagation modulated by the absorption ($\sigma_a(\lambda)$) and scattering ($\sigma_s(\lambda)$) cross-sections with a unit of L^2 and which are both functions of wavelength. In this approach, a local interaction of the radiation with the medium is considered

by these parameters which are statistical approximations of actual physical processes. This approach is especially useful for modeling light propagation in a medium where the heterogeneity is significantly high. Typical tissue contains particles between 1 and 1000 μm [43]. On the other hand, at the macroscopic scale, absorption and scattering processes are modeled as linear absorption ($\mu_a(\vec{r},\lambda)$) and scattering ($\mu_s(\vec{r},\lambda)$) coefficients of the medium with the unit of $[L^{-1}]$. They are derived by formulas [44]:

$$\mu_a(\vec{r},\lambda) = \rho_a(\vec{r}).\sigma_a(\lambda) \tag{2.4}$$

$$\mu_s(\vec{r},\lambda) = \rho_s(\vec{r}).\sigma_a(\lambda) \tag{2.5}$$

in which $\sigma_a(\lambda)$ and $\sigma_s(\lambda)$ are absorption and scattering cross-section of a molecule/atom and $\rho_a(\vec{r})$ and $\rho_s(\vec{r})$ are concentrations of absorbing and scattering material $[L^{-3}]$. As The formulas 2.4 and 2.5 imply spatial averaging due to local densities of absorbers and scatterers are preferred. This approach of averaging of optical properties of the medium can be safely used in biomedical optics. Generally, the region-of-interest in optical imaging is soft tissue as a bulk in the centimeter-scale thus abrupt deviations in homogeneity of soft tissue is rare [6]. Hence it is possible to calculate light-tissue interaction or light propagation when the interrogated medium is bulk [43] which is typical in DOT, fNIRS, OCT applications. Hence, these calculations use continuum models of light propagation for which $\mu_a(\vec{r},\lambda)$ and $\mu_s(\vec{r},\lambda)$ are sufficient as inputs. Another advantage of the macroscopic-averaging approach is its usefulness in the preparation of tissue-simulating phantoms. Experiments with phantoms require tissue-simulating media with different optical properties. Utilization of various absorbers and scatterers with known concentrations and optical properties results in definite scattering and absorbing characteristics for reproducible and controlled experiment stances.

A more detailed formulation of scattering coefficient has been achieved by a simple monodisperse model of scattering dielectric spheres:

$$\mu_s^{'}(\vec{r},\lambda) = 3.28\pi a^2 \rho_s(\vec{r}) (2\pi a/\lambda)^{0.37} (m-1)^{0.29} \tag{2.6}$$

where, a is the sphere radius, $\rho_s(\vec{r})$ is the concentration of spheres and m represents the ratio of refractive index of embedded scatterers to that of the background medium [5].

As it can be deduced from Eq. 2.4 and Eq. 2.5, this approach for modeling of absorption and scattering do not involve any angular dependence with respect to angle of incidence. However there exists tissue types with directional alignment [45–47], e.g. myofibrils in the muscle, collagen fibers lying parallel to the skin surface. Researchers studied both experimentally and computationally the characteristics of the anisotropy of absorption and scattering properties of the medium. It has been reported experimentally that reflectance measurements are mostly affected by the anisotropy of scattering [46]. In Fig. 2.2, an example of reflectance measurement on the abdomen at a distance of 5 mm. from the source is shown. Measurement is done in a polar coordinate system, in which angle range is [0°,360°] and each polar line represents iso-intensity of measured light. In the same study [46], it is reported that anisotropy is radius dependent. In Figure 2.3, reflectance measurements for different source-detector distances are shown. In both cases, anisotropy of optical properties clearly seems to affect the reflectance.

Another important aspect in the modeling of scattering is the angular distribution of secondary radiation due to a single scattering event, because an adequate model of light propagation necessitates it. The term used for the function defining angular distribution of a single-scattering event is scattering phase function (SPF). A useful simplifying parameter is the mean cosine of cumulative scattering [49]:

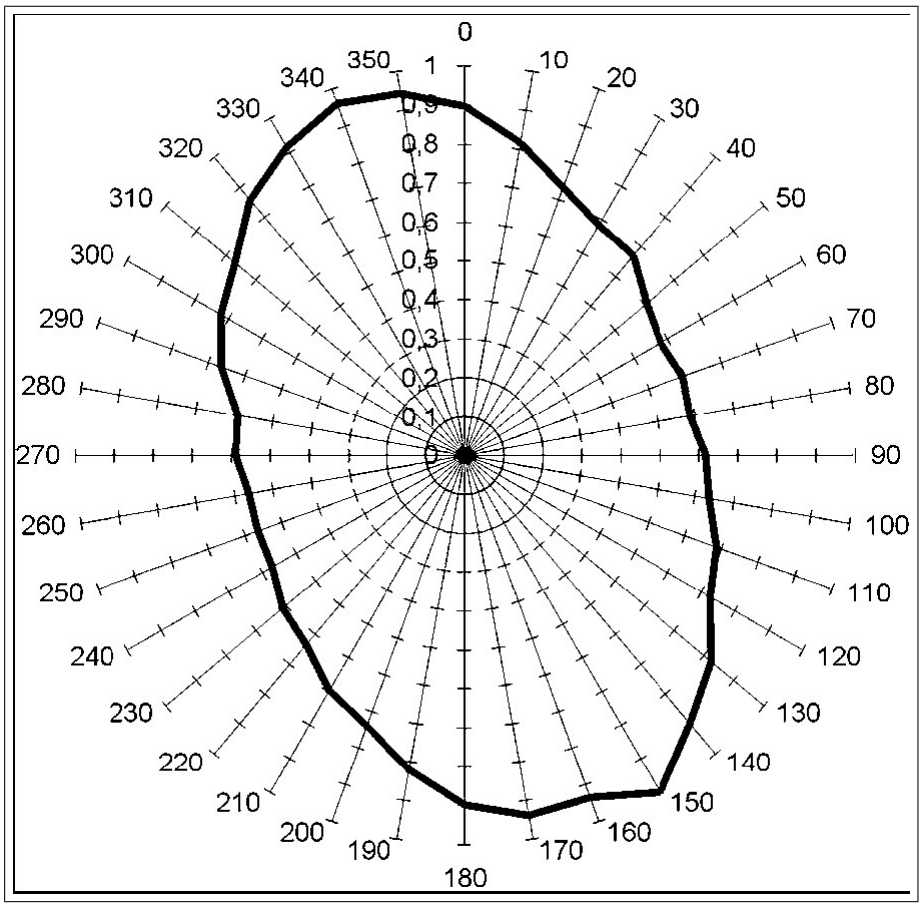

Figure 2.2 Reflectance measurement on the abdomen where source detector distance is 5 mm. In this polar diagram, the distance from the center in each direction represents the reflectance measured at that angle [18] [48].

$$\langle \cos(\theta) \rangle = \int S(\theta) \cos(\theta) \, d(\cos(\theta)) \tag{2.7}$$

in which $S(\theta)$ symbolizes normalized SPF. The range of mean cosine is $[-1 + 1]$, ranging from backward to forward-peaked scattering respectively. Specifically, a value of zero for the mean cosine means the scattering of the medium is isotropic with equal probability of being scattered in every direction over 4π site radians.

In soft tissue, there are various and numerous morphological features which can influence light scattering. The changes in the refractive index due to cell boundaries and the presence of intracellular organelles, such as cell nuclei and mitochondria are

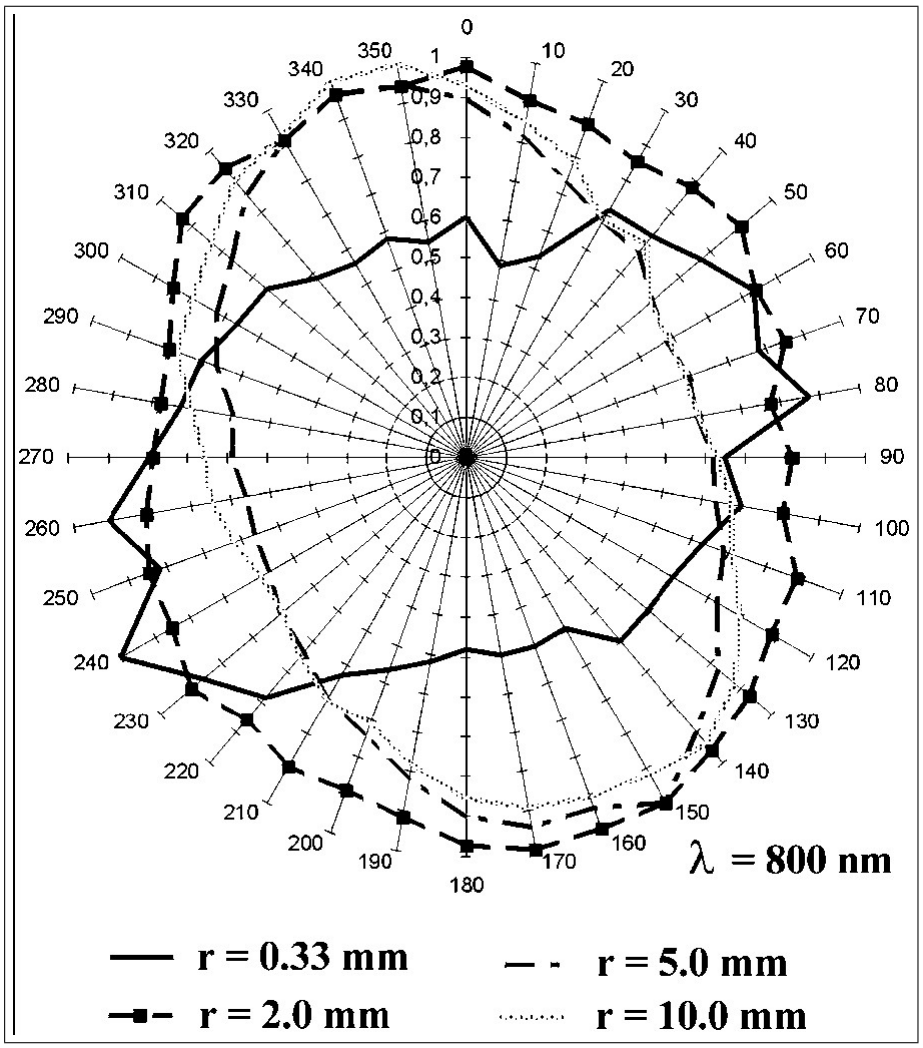

Figure 2.3 Reflectance measurement on the abdomen for different source-detector distances. In this polar diagram, the distance from the center in each direction represents the reflectance measured at that angle [18], [48].

among such influences. The variety and complexity of these influences make modeling an average scattering interaction problematic. Unknown size and distribution of the scattering agents results in more unknowns. An averaging over volume similar to the modeling of absorption and scattering coefficients can be utilized for the SPF also, namely volume scattering function [50]. In this method the scattering spread of single-scattering events of living tissue are measured by single-photon counters in a goniometric apparatus as shown in Figure 2.4 [49–52]. The sample is placed as a very thin slice to avoid multiple scattering events [49–52]. Results of measurement of volume scattering are given in Figures 2.5 and 2.6 [49–52].

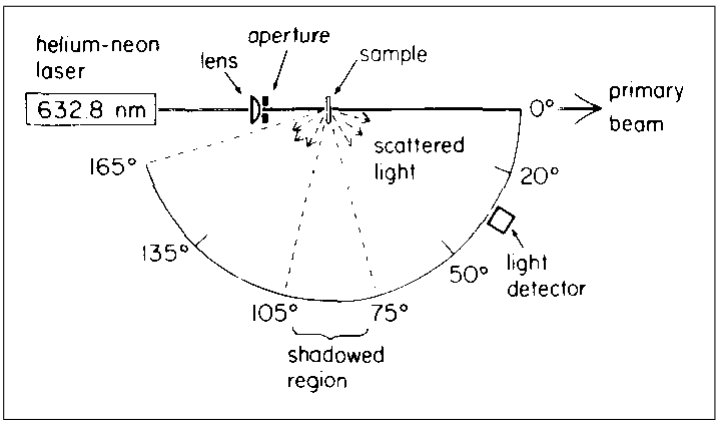

Figure 2.4 A schematic view of goniometric measurement of phase function of tissue sections. A thin tissue sample is exposed to laser beam [52].

Measurement of phase functions indicates that scatterers of living tissue (soft) have forward-peaked scattering properties. In the experiments very thin slices of samples are used to avoid multiple scattering, hence results of the experiments can be considered as a statistical distribution of scattering characteristics of a single scattering event. A forward-peaked pattern suggests that size of scatterers of living tissue is of the same size or bigger than the wavelength used (632.8 nm and 783 nm in these particular cases). Mie's scattering theory by spherical particles give a result of >0.5 μm for the average diameter of the scatterers [49].

The ways to represent a single-scattering event to be used in light propagation modeling are various. Though some researchers use empiric formulations for SPF [50] in Figure 2.6, more generally adaptation of mathematical expressions from astrophysics Henyey-Greenstein (HG), scattering theories like Rayleigh-Gans (RG), Mie are used (Figure 2.7).

HG phase function is:

$$P_{HG}(\theta) = \frac{1}{4\pi} \frac{(1-g^2)}{(1+g^2-2g\cos(\theta))^{\frac{3}{2}}} \tag{2.8}$$

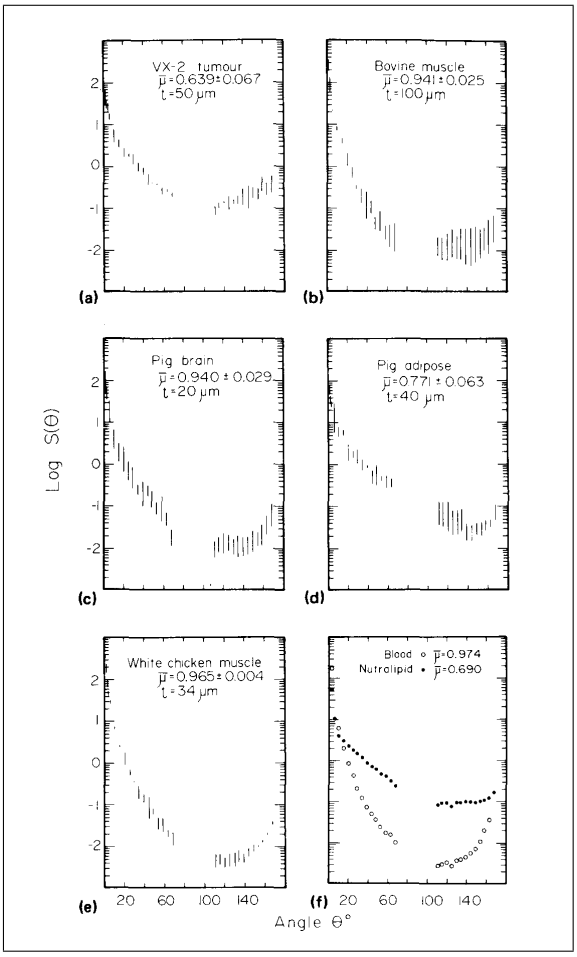

Figure 2.5 Measurement of phase functions of tissue at 632.8 nm. [49] [52].

where θ is the difference between the angle of photon before it is scattered and after it is scattered (deflection angle) and g is defined as:

$$g \equiv \langle \cos(\theta) \rangle = \int_0^{\pi} \cos(\theta)\, P_{HG} 2\pi \sin(\theta)\, d\theta \tag{2.9}$$

It has reported that HG phase function describes single scattering in tissue very well.

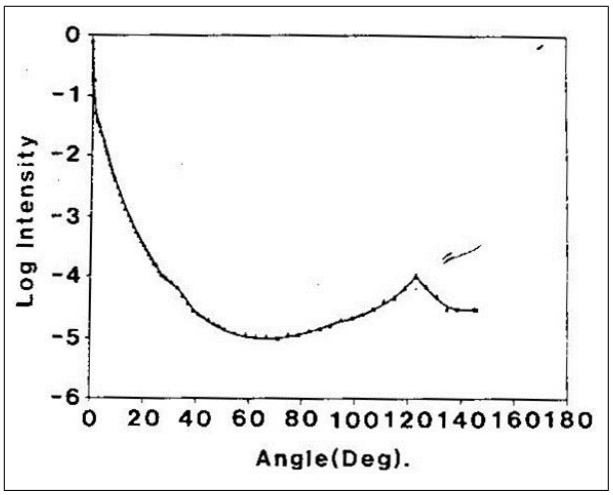

Figure 2.6 Averaged SPF for human red blood cells at 783 nm. The sharp peak at 120° is an instrumental artifact [50].

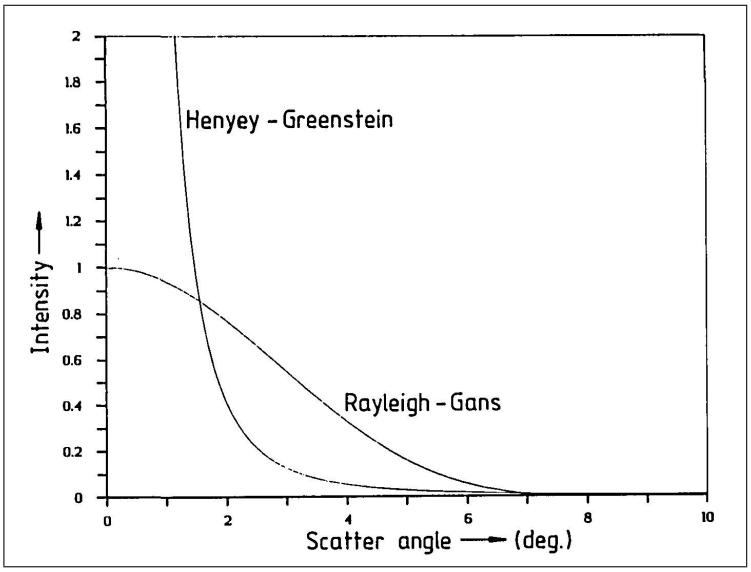

Figure 2.7 Raygleigh-Gans and Henyey-Greenstein angular scattering distributions for single scattering and g = 0.995 [53].

In biomedical optics, HG phase function has been used for modeling light propagation since 1976 [54]. It was originally proposed by HG for stellar scattering. Even though, it has been reported that there are significant discrepancies between average cosine of scattering calculated by HG and that by Maxwell equations, it is commonly implemented in the modeling of light propagation [55] [56]. The main reasons behind this fact are; it is a "far simpler expression´´ relative to other phase functions, has reasonably good agreement between Mie scattering below average cosine of 0.8 and it

can be solved for scattering angle in closed form [54]. In Figure 2.8 the measurement of laser beam deflection for different thickness of tissue samples (in this case human skin) is shown. As the sample thickness approaches zero, forward deflection is evident which means scattering in tissue is forward deflected [57]. In Figure 2.9. a comparison of Mie scattering function and HG function is shown. In this case the discrepancy between these formulations is significant especially when the scattering angle is close 0^{o}.

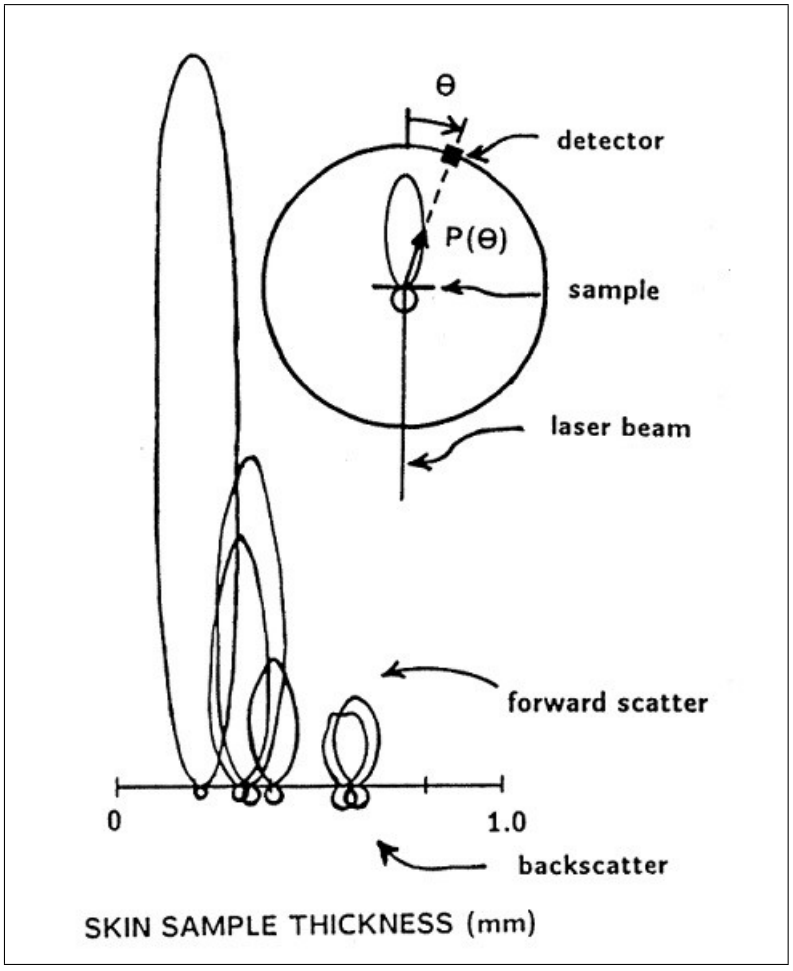

Figure 2.8 Deflection angle measurements for different thickness of skin samples for He-Ne laser [57].

Further studies [46] [58] [59] have elucidated another negative aspect in the use of HG. Eq. 2.7 shows the distribution of scattering angles in single scattering events in the exact formulation. In Monte-Carlo simulations calculation of cosine of the scattering angle ($\cos(\theta)$) is more important than calculation of the scattering angle directly to speed up the computation [55] [56]. Hence it has been proposed that it is feasible to use HG phase function in another form where cosine of scattering angle is

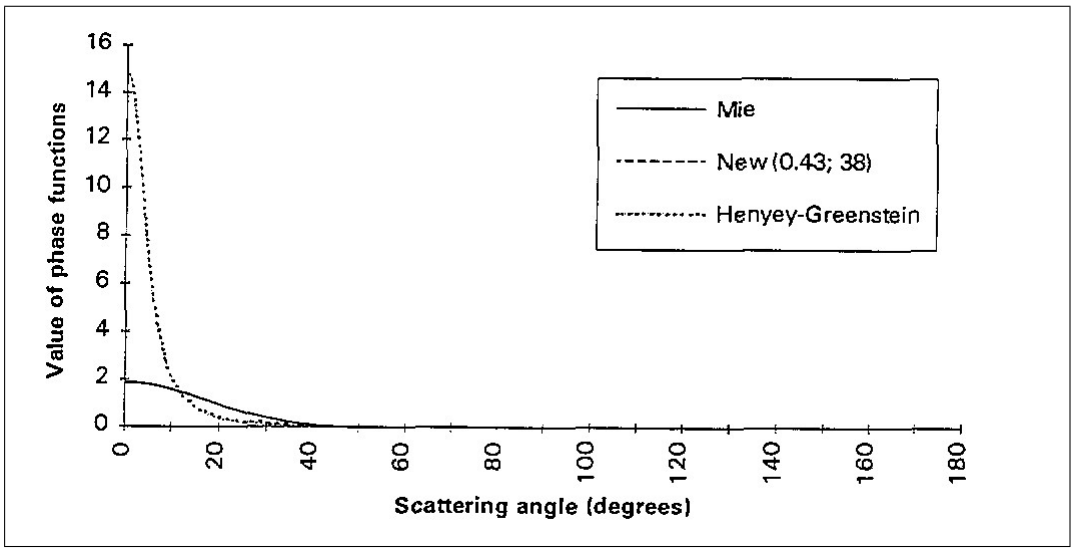

Figure 2.9 Comparison of phase functions from Mie theory and Henvey-Greenstein calculations for g value of 0.995 [54].

sampled instead of the angle [46] (Eq.2.10):

$$P_{HG}(\theta) = \frac{1}{2}\frac{(1-g^2)}{(1+g^2-2g\cos(\theta))^{\frac{3}{2}}} \tag{2.10}$$

where g is the average of scattering angles (anisotropy factor of the phase function) which can be solved for $\cos(\theta)$ in closed form:

$$\cos(\theta) = \left\{ \begin{array}{cc} \frac{1}{2g}\left[1+g^2-\left(\frac{1-g^2}{1-g+2g\xi}\right)^2\right] & if\, g \neq 0 \\ 2\xi - 1 & if\, g = 0 \end{array} \right\} \tag{2.11}$$

This form has been used for decades in biomedical optics. However, some discrepancies have been reported [46] for sampling of scattering angle $\cos(\theta)$ by the exact formula given in Eq. 2.10 (Figure 2.10) and Eq.2.11.

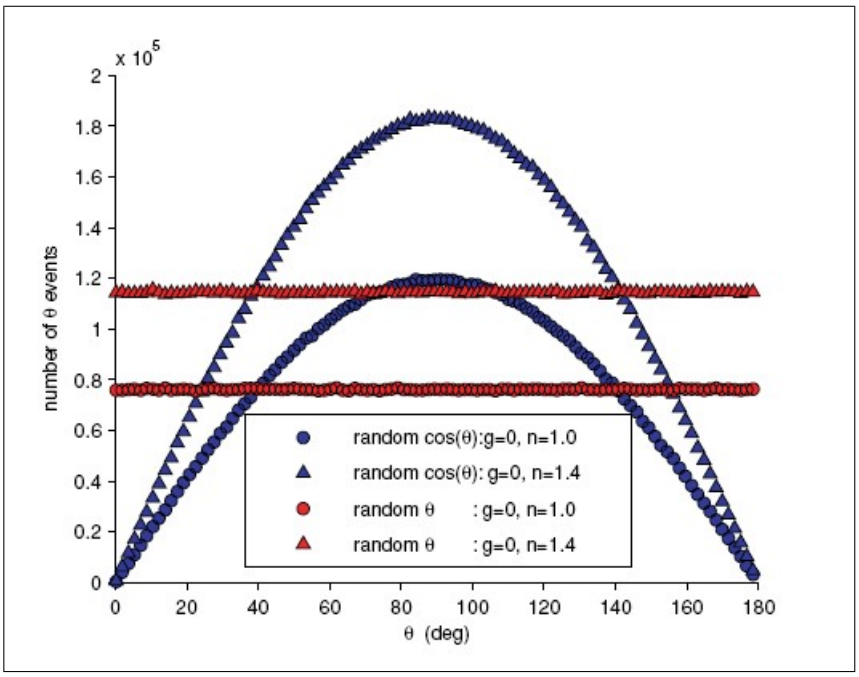

Figure 2.10 Histograms of the scattering angles θ in degrees for four distinct MC simulations. Random $\cos(\theta)$ means that the $\cos(\theta)$ of has been generated during the Monte Carlo simulations. Random θ means that θ has been directly generated during the Monte-Carlo simulation [46].

However, it has been shown that a comparison of different forms of HG functions are not meaningful [58]. If the formula given by Eq. 2.10 is accepted as a probability density function (probabilistically to be used stochastic approaches) for the deflection in zenith and assuming that scattering in azimuth is of equal probability, photon distribution on a sphere around a scattering center is to be uniform for isotropic scattering events. Hence, the correct formula to be used is the one given in Eq. 2.11. The formula given in Eq. 2.7 must be modified as given below (Eq. 2.12) to satisfy the condition of uniform photon distribution over a sphere enclosing a scattering center for isotropic scattering.

$$P_{HG}(\theta) = \frac{1}{4\pi} \frac{(1-g^2)\sin(\theta)}{(1+g^2-2g\cos(\theta))^{\frac{3}{2}}} \tag{2.12}$$

The intensity of back scattered light from a tissue by simulations depend on the phase function used [59]. A comparison of experimental data with simulated data by

Mie and HG phase functions indicates that for small source-detector separations (sub-millimeter) results of simulations with HG phase function deviates from experimental data. However, for large source-detector distances, simulations with phase functions give similar results [59]. A possible explanation of this phenomenon is the different scattering characteristics of Mie and HG phase functions (Figure 2.11). Mie scattering function reflects higher backwards scattering than HG does [59]. This difference is more pronounced when the source-detector distance is small. For larger distances, the randomization of directions of photons propagating inside the medium is so effective that diminishes the difference. A qualitative measure of this effect has been given by Canpolat [59] defining the extent of effect as the region where the product of scattering coefficient, source-detector distance and $(1 - g)$ is below two.

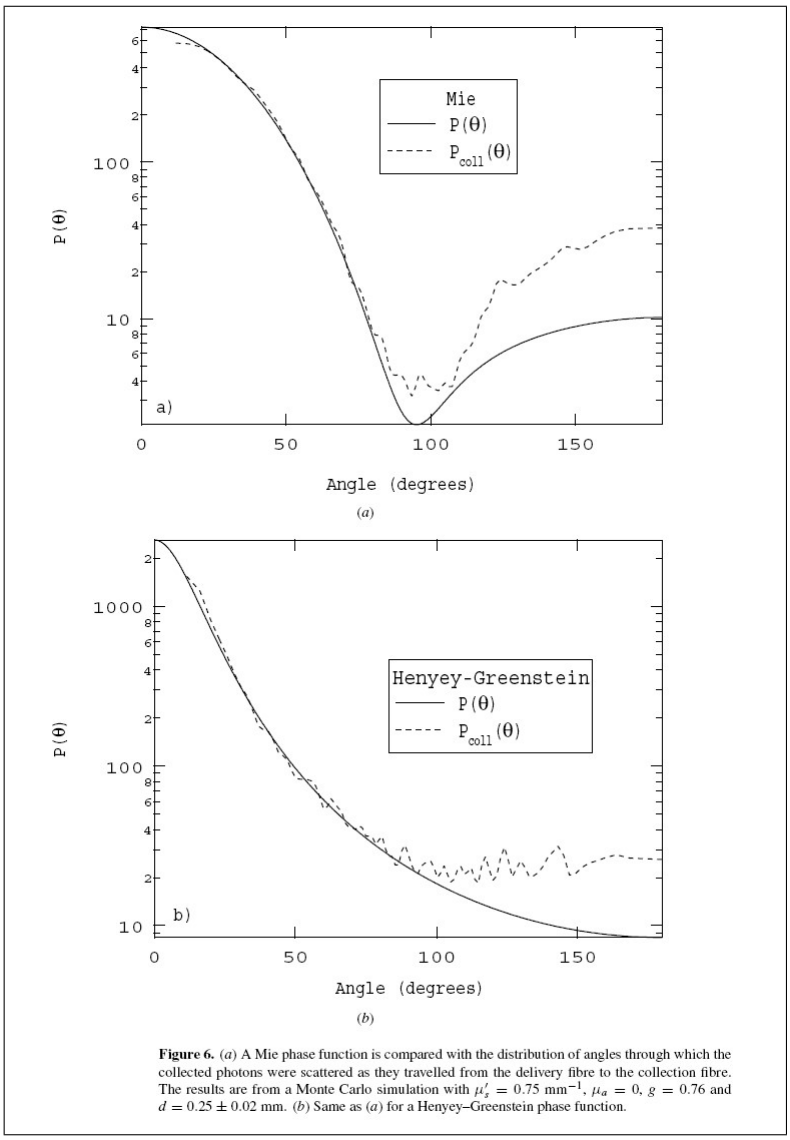

Figure 6. (*a*) A Mie phase function is compared with the distribution of angles through which the collected photons were scattered as they travelled from the delivery fibre to the collection fibre. The results are from a Monte Carlo simulation with $\mu_s' = 0.75$ mm^{-1}, $\mu_a = 0$, $g = 0.76$ and $d = 0.25 \pm 0.02$ mm. (*b*) Same as (*a*) for a Henyey–Greenstein phase function.

Figure 2.11 Different scattering characteristics of Mie and HG phase functions [59].

2.4 Light Propagation in soft tissue (turbid media) revisited

In Figures 2.12 - 2.16 a series of experiments on light propagation in different circumstances are shown. Figure 2.12 shows the light pattern in a dilute starch solution. From Figure 2.12 to Figure 2.16 hematocrit concentrations are 0.005, 0.014, 0.046, and 0.20 respectively. Even though, this experimental setup is not exactly the same as realistic cases in which tissue is made up of many different types (turbid media), it ascertains that light propagation in turbid medium is transformed into a diffusion-like

character by multiple scattering. As scattering coefficient of a medium is relatively high, multiple scattering of EM radiation changes propagation into a scheme where coherence among wavelets is lost. Further polarized light can keep its polarization as long as a few free mean paths which is the mean of path lengths taken by photons without an interaction. In this case even though Maxwell's equations (vector) are linear equations where fields are additive, light propagation becomes a power-additive case (scalar) which is named as radiative transfer [60]. The properties of light propagation also elucidate the effect of scattering coefficient of medium on light propagation clearly. Scattering coefficient of media is ascending for cases in Figures 2.12 to 2.16, scattering coefficient modulates light into a diffuse character. Besides scattering coefficient, it can be deduced intuitively that absorption coefficient mostly alters the extent of penetration of light into the medium.

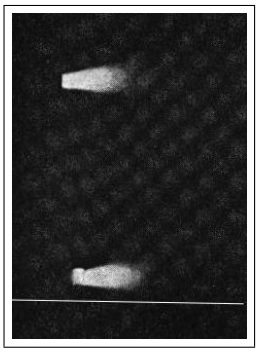

Figure 2.12 Light pattern in a dilute starch solution [61].

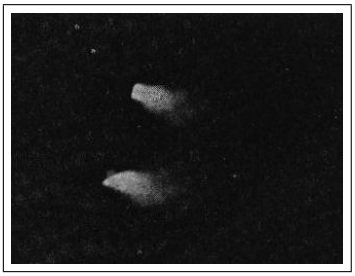

Figure 2.13 Light pattern in blood with H = 0.005 [61].

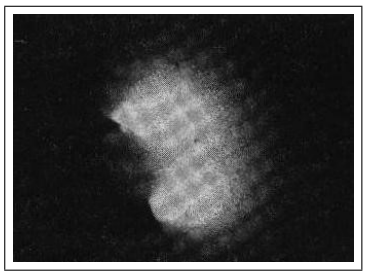

Figure 2.14 Light pattern in blood with H = 0.014 [61].

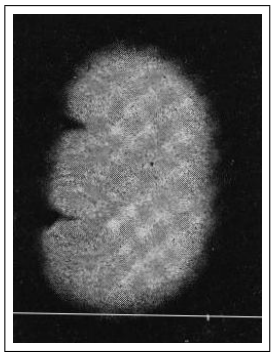

Figure 2.15 Light pattern in blood with H = 0.046 [61].

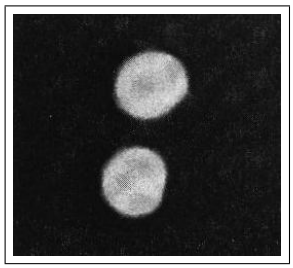

Figure 2.16 Light pattern in blood with H = 0.20 [61].

As aforementioned in Eq. 2.7, scattering in soft tissue is the result of refractive index mismatches within the tissue. Hence it is deduced that when the refractive-index-mismatch is reduced, diffusive character of photon propagation can be reduced. In Figure 2.17, two suspensions of Rhodopseudomonas spheroids are shown in two different media. On the left side of the Figure 2.17, the text on the paper could be read, which is not possible on the right-hand side. Propagation of photons in a medium where refractive-index-mismatch is reduced, photons follow straight paths enabling the reading of the paper placed behind the tubes [62].

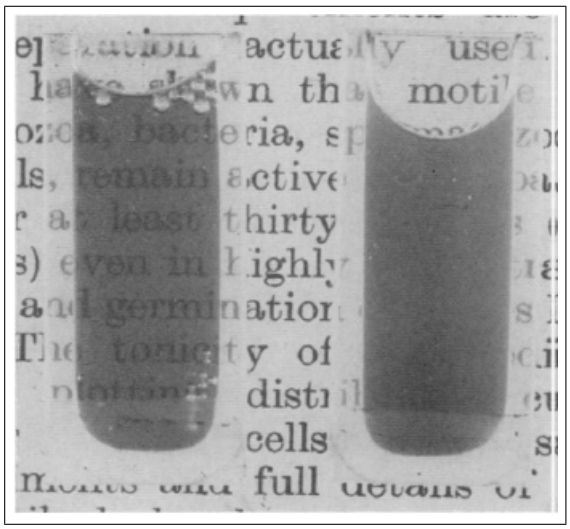

Figure 2.17 The suspension on the left has a refractive-index-matched solute and medium where the solute is Rhodpseudonomas spherodes and the medium is a protein solution. On the right-hand side, the solution is aqueous culture. Both tubes contain the same number of cells per unit volume [62].

2.4.1 General Aspects of NIR light propagation in soft tissue

The propagation of NIR light in soft tissue is dominated by scattering. As it is shown in Figure 2.18, the absorption of tissue constituents are relatively low for this portion of spectrum, thus light can penetrate several centimeters inside the living tissue [6].In vivo optical properties of various living tissue are given [5]. Generally speaking, living (soft) tissue reflects NIR photons multiply without a change in its wavelength (elastically), and absorbs in minute amounts resulting in a diffusion-like propagation. However, there are tissue components like cerebro-spinal fluid (CSF) where NIR light is not multiply scattered and not absorbed significantly. Modeling of light propagation in clear regions is drastically different than that of multiply-scattering regions [63–65].

It is very well known that propagation of photons (or EM waves) is not affected by the presence of each other. In other words, the probability that a photon will travel a certain distance is not influenced by the presence of other photons. Therefore, equations governing photon diffusion must be linear in the density of photons per volume. This property will be exploited for obtaining approximate solutions in a medium where optical properties of the medium are not changed by the side effects of light-tissue

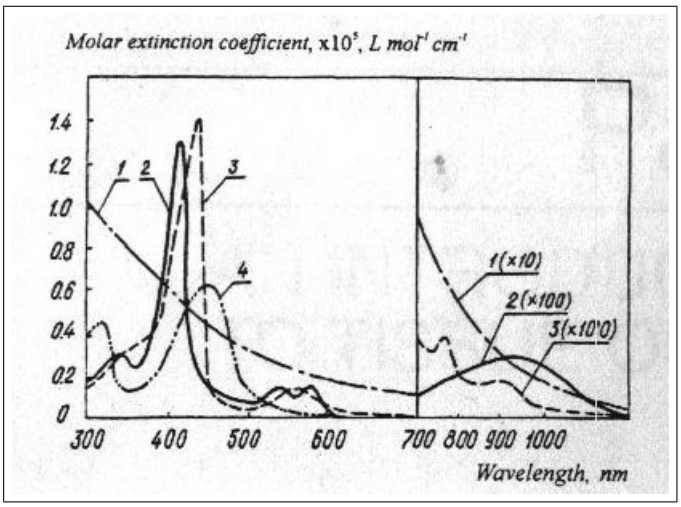

Figure 2.18 Molar attenuation spectra for solutions of major visible light-absorbing human skin pigments: 1-Dopa Melanin, 2-oxyhemoglobin 3- hemoglobin 4- bilirubin [5].

interaction such as heating due to absorption. In biomedical applications light intensity is adjusted to safe level to avoid hazardous heating effects. Hence, it can be deduced that in biomedicine tissue is optically static (in terms of optical properties of scattering cross section or absorption cross section).

2.4.2 Modeling aspects of NIR light propagation in soft tissue

Modeling of NIR propagation in highly-scattering media by scalar theories can be handled in various ways. A general approach named radiative transfer theory depending on Boltzmann?s transport equation [66] [67] (namely Radiative Transfer equation (RTE)) is used. Even though this approach is of general applicability from turbid media to clear regions, its integro-differential form grounds difficulties in the pursuit of its solution. Approximations of RTE which more soluble equations have been developed with the trade of squeezing the generality.

2.4.2.1 Radiative Transport Approach. This approach depends extensively on transport theory developed by Boltzmann [68]. The main physical quantity defined is specific intensity or radiance which is generally represented by capital I in

biomedical applications. In nuclear reactor calculations, and statistical mechanics it is named as angular distribution [68] and represented by f. It is a scalar function of time, space and direction [66] [68] representing the number of photons at position $\tilde{r}$, at time t and moving in a direction $\hat{s}$. In Figure 2.19, scattering of specific intensity in a volume element ds is shown.

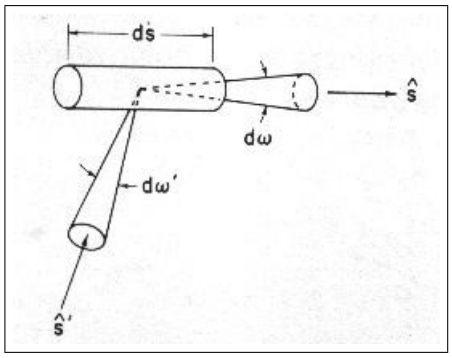

Figure 2.19 Scattering of specific intensity upon the volume ds from the direction into the direction [66].

First a time-independent formulation of modulation of specific intensity can be formulated as follows.

$$dI\left(\vec{r},\hat{s}\right) = -ds\left(\mu_a + \mu_s\right) I\left(\vec{r},\hat{s}\right) \tag{2.13}$$

where μ_a and μ_s are absorption and scattering coefficients respectively. Specific intensity in the direction of decreases due to both scattering and absorption [66]. However, since the medium is highly scattering, some contributions from scattering occurring inside the ds is added to specific intensity which is directly proportional to scattering properties. Hence time-independent radiative transfer equation (RTE) becomes (2.14):

$$\hat{s}\cdot\vec{\nabla} I\left(\vec{r},\hat{s}\right) = -(\mu_a + \mu_s) I\left(\tilde{r},\hat{s}\right) + q\left(\tilde{r},\hat{s}\right) + \mu_s \int f\left(\hat{s},\hat{s}',\tilde{r}\right) I\left(\tilde{r},\hat{s}'\right) d^2\hat{s}' \tag{2.14}$$

In Eq. 2.14, $q(\vec{r},\hat{s})$ represents source term, scattering phase function. In the time-dependent regime, a term to represent time dependence of I is added to the Eq. 14, and source term also becomes time-dependent. Consequently time-dependent RTE is given as :

The equation (Eg. 2.15) depends on (local) optical properties and SPF of the medium.

$$\hat{s}\cdot\vec{\nabla}I(\vec{r},\hat{s},t)+\frac{\partial I(\vec{r},\hat{s},t)}{\upsilon\partial t}=-(\mu_a+\mu_s)I(\vec{r},\hat{s},t) + q(\vec{r},\hat{s},t)+\mu_s\int f(\hat{s},\hat{s}',\vec{r})I(\vec{r},\hat{s}',t)\,d^2\hat{s}' \quad (2.15)$$

Selection of an appropriate phase function enables one to calculate light propagation with a significant anisotropy [66]. Even though this formalism is reliable in most cases, this integro-differential equation is difficult to solve except some idealized cases and simple biological structures [5] [13]. Another shortcoming of this formalism is the definition of appropriate boundary conditions structures [5] [13] which is a difficult task.

Alternative rephrasing of light propagation can be given as [69] time dependent by specific intensity $I(\tilde{r},\hat{s},t)$ (Eq. 2.16) [14] and its counterpart in frequency domain (Eq. 2.17) [15]:

$$\left(\frac{1}{\upsilon}\frac{\partial}{\partial t}+\hat{s}\cdot\vec{\nabla}+\mu_{tr}(\vec{r})\right)I(\tilde{r},\hat{s},t)=\mu_s(\vec{r})\int f(\tilde{r},\hat{s},\hat{s}')I(\tilde{r},\hat{s},t)\,d\hat{s}'+q(\tilde{r},\hat{s},t) \quad (2.16)$$

$$\left(\frac{i\omega}{c}+\hat{s}\cdot\vec{\nabla}+\mu_{tr}\left(\vec{r}\right)\right)I\left(\tilde{r},\hat{s},\omega\right)=\mu_{s}\left(\vec{r}\right)\int f\left(\tilde{r},\hat{s},\hat{s}'\right)I\left(\tilde{r},\hat{s},w\right)d\hat{s}'+q\left(\tilde{r},\hat{s},w\right) \tag{2.17}$$

where $\mu_{tr}\left(\vec{r}\right)=\mu_{a}\left(\vec{r}\right)+\mu_{s}\left(\vec{r}\right)$

2.4.2.2 Diffusion Approximation to radiative transfer. Diffusion approximation to radiative transfer is applied to biomedical optics in many studies [5] [70–75]. The main motivation to implement approximation is to derive an equation which can be more easily solved with respect to Eq. 2.15. As it is explained above the formulation found must be linear in photon concentration. Hence, obtaining diffusion approximation in the form of a differential equation is desirable at the expense of limited applicability with respect to Eq. 2.15.

If scattering events are assumed to be isotropic leading to a uniform angular distribution, no net energy would be propagated through any surface present in the region-of-interest, because net flow of photon energy through any unit surface throughout the medium would be diminished by equal amounts of energy passing the surface from opposite directions. This situation is an equilibrium state in photon density which is not realistic because photon sources and absorption will change the photon distribution. Furthermore, the aim of optical methods is to interrogate deep tissue layers by remote illumination in the order of several centimeters. Experimentally light propagation has been reported as a net flow of several centimeters inside a turbid medium. Therefore, the solution of diffusion equation must govern physical situation when photon density is at "nearly" equilibrium all over the space in which a minute amount photon energy transfer can shatter the equilibrium.

Such a situation is reached when a soft tissue is illuminated by NIR photons. When photons are injected into a turbid medium via a point source they experience multiple scattering without being absorbed significantly, therefore an "almost" equilib-

rium state is reached [66] [76]. Under these circumstances, angular scattering is also almost isotropic. To achieve this case scattering coefficient must be very large with respect to absorption coefficient. Hence (diffuse) specific intensity can be modelled as a summation of two components:

$$I_d\left(\tilde{r},\hat{s}\right) = U_d\left(\tilde{r}\right) + \left(\frac{3}{4\pi}\right)\vec{F}_d\left(\vec{r}\right)\cdot\hat{s} \tag{2.18}$$

where $\tilde{F}_d\left(\tilde{r}\right)$ is diffuse flux vector (direction is given by a unit vector). (Figure 2.20)

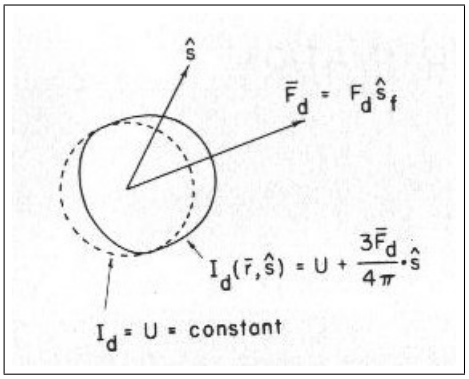

Figure 2.20 Diffuse intensity Id for diffusion approximation. Diffuse intensity is summation of two components: a U (constant) term and a directed term. [6]

This modeling leads to diffusion approximation (DA) of radiative transfer equation in both time-domain (2.19) and frequency domain (2.20) [69]:

$$-\tilde{\nabla}\cdot\kappa\left(\tilde{r}\right)\tilde{\nabla}\Phi\left(\tilde{r},t\right) + \mu_a\left(\tilde{r},\lambda\right)\Phi\left(\tilde{r},t\right) + \frac{1}{c}\frac{\partial\Phi\left(\tilde{r},t\right)}{\partial t} = q_0\left(\tilde{r},t\right) \tag{2.19}$$

$$-\tilde{\nabla}\cdot\kappa\left(\tilde{r}\right)\tilde{\nabla}\Phi\left(\tilde{r},\omega\right) + \mu_a\left(\tilde{r},\lambda\right)\Phi\left(\tilde{r},t\right) + \frac{i\omega}{c}\frac{\partial\Phi\left(\tilde{r},\omega\right)}{\partial t} = q_0\left(\tilde{r},\omega\right) \tag{2.20}$$

in which $\Phi(\tilde{r}, t)$ is photon density, $\kappa(\tilde{r})$ is the diffusion coefficient, λ is the wavelength of the source and q_0 is isotropic source. Photon density and diffusion coefficient are given by:

$$\Phi(\tilde{r}, t) = \int_{4\pi} I(\vec{r}, s, t)\, d^2 s \tag{2.21}$$

$$\kappa(\tilde{r}, \lambda) = \frac{1}{3\left(\mu_a(\vec{r}, \lambda) + \mu_s(\vec{r}, \lambda)(1-g)\right)} \tag{2.22}$$

where $\mu_{st} = \mu_s(1-g)$ is named as reduced or transport scattering coefficient.

The set of equations in Eq. 2.16 and Eq. 2.17 are describing photon migration exactly if an appropriate phase function and the set of boundary conditions are imposed. In the case of diffusion approximation, equations govern the case where the scattering is almost isotropic. The resulting formula do not involve any scattering phase function. Also, transport theory equations 2.16 and 2.17 involve scattering and absorption coefficient to include light-tissue interactions, but DA equations on the other hand involve only the diffusion coefficient Eq. 2.19 and Eq. 2.20. The validity of DA equations are limited where photons are multiply scattered and the orientation of photons are randomized enough that scattering is almost isotropic. Intuitively, the space interrogation close to source and surfaces are the volume where DA equations are not valid. Recently, the borders of validity for slab geometries and for source-detector distances have been reported. In slab geometry, if the ratio of thickness of the slab z to transport mean path l is small, diffusion theory do not predict corrected values for light propagation in turbid media. Particularly, $\frac{z}{l}$ is less than 10 for a slab thickness of 10 mm, significant discrepancies start to be seen between results of DA and exact theories [77]. The validity of DA is diminished if the product of reduced scattering coefficient and distance is below two [59]. It is known that DA breaks down in the re-

gion close to surfaces. In Figure 2.21, a comparison of photon density as a function of depth is shown. Dashed line symbolizing approximate solution by DA equation seems to deviate from that of exact solution (solid line in Figure 2.21) significantly at the region close to surface. Generally speaking if the direction of propagation of photons is not randomized enough, DA is not proper to use.

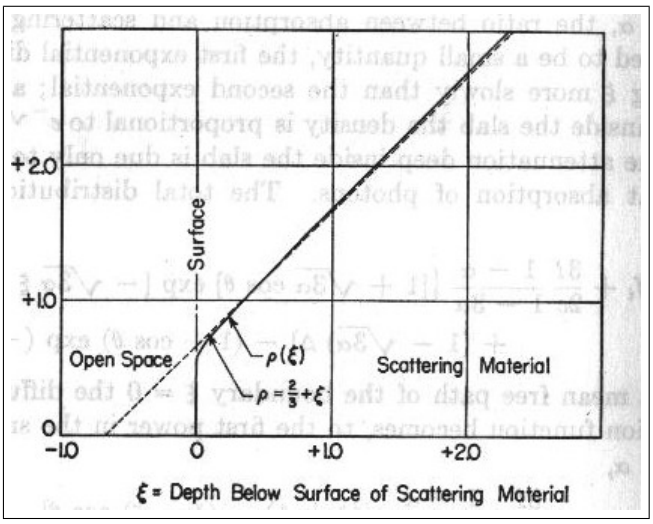

Figure 2.21 Density of photons as the function of depth inside a scattering medium. Near surface of the scattering medium. Dashed line shows approximate solution, and solid line is for the exact solution [78].

2.5 General properties of Monte-Carlo Simulation of Photon Migration in Turbid Media

Even though Monte Carlo (MC) simulation of photon migration in turbid media is not used this study, its inclusion is would be beneficial since MC simulation is the gold standard in biomedical optics studies.

Various physical problems have been solved by Monte-Carlo simulations. In a typical MC simulation step first is to construct a stochastic model of the actual physical phenomena. Then, multiple independent samples are obtained. They are of probabilistic character; they offer flexible and rigorous approach to many physical situations. Like other stochastic methods, they also incorporate noise directly.

2.5.1 Monte-Carlo Simulation of Photon Propagation In Turbid Medium

In a MC simulation, it is assumed that photons are ballistic particles. Therefore phenomena such as coherence and interference effects can be ignored and only motion

of a photon between photon-medium interaction sites (PMIS) (step size), hitting a boundary between a layer/layer and layer/ambient-layer, scattering and absorption are considered. Optical properties of the medium are defined only by the absorption coefficient, the scattering coefficient, and the angular intensity distribution of a single scattering (i.e. the scattering phase function) event. Other effects such as fluorescence are ignored. The phase function depends only on the relative angle of scattering. Scattering does not affect the energy of a photon, in other words, scattering is elastic. The optical properties of the medium are not chanced by the absorption of photons.

Values for the considered variables for a photon are determined randomly from probability distributions. For a random variable χ, e.g. photon step size, there exits a probability density function $p(\chi)$ defining the distribution of χ over the interval. So as to choose a value for any variable the equation below is solved since there are pseudo-random generators to provide us with a random number with a range of $(0, 1)$ with uniform distribution. This allows us to produce a value of any variable repeatedly and randomly.

$$\int_a^{\chi} p(\chi)\, d\chi = \xi, \xi \in (0, 1) \tag{2.23}$$

The physical properties attributed to photons are (1) a step size determining the distance of its next motion till scattering happening at the next photon-matter interaction site, (2) a weight (shown as W in the text) at the beginning of their launch into slab which diminishes due to absorption. Since they move inside the slab in three dimensions, they are also given three directional cosines with respect to a Cartesian coordinate system residing at the origin of the slab (the point where photons are injected). Each photon is tracked with three spatial coordinates.

Simulation starts by launching a photon, normally injected onto the slab at the origin with the shape of infinitely narrow beam of photons. The position of the

photon is initialized to (0,0,0). Directional cosines are adjusted to (0,0,1). Weight (W) is initialized to 1. Since there could be mismatched boundary between the first layer of the slab and ambient layer, specular reflectance is included in the code. Specular reflectance is formulated as [79]:

$$R_{sp} = \frac{(n_1 - n_2)^2}{(n_1 + n_2)^2} \tag{2.24}$$

At this step, the weight of the photon which is initialized to 1 is decreased by specular reflectance. This decrement is given with the expression below:

$$W = 1 - R_{sp} \tag{2.25}$$

next, the photon is moved to the PMIS. Firstly, step size of PMIS is to be determined. It depends on a sampling of the probability distribution for the photon?s free path $s\,(0 \leq s \leq \infty)$. Interaction coefficient $\mu_t (= \mu_a + \mu_s)$, the probability of photon-medium interaction per unit pathlength in the interval $s', s' + ds'$, which is shown as $P\,(s \geq s')$, and is defined as:

$$\mu_t = \frac{-dP\,\{s \geq s'\}}{P\,\{s \geq s'\}\,ds'} \tag{2.26}$$

or in other form:

$$d\,(ln\,(P\,\{s > s'\})) = -\mu_t ds' \tag{2.27}$$

We use the equation below to determine the step size of a photon depending on the principles above, where s is the step size, μ^t is interaction coefficient, and is a random number generated by a computer:

$$s = \frac{-ln\,(\xi)}{\mu_t} \tag{2.28}$$

After defining step size of the photon, now the photon can be moved. The location of the photon packet is changed according to the set of equations below:

$$x = x + \mu_x s \tag{2.29}$$

$$y = y + \mu_y s \tag{2.30}$$

$$z = z + \mu_z s \tag{2.31}$$

Once a photon reaches an interaction site, a fraction of its weight is absorbed by the interaction site according to:

$$\Delta W = \left(\frac{\mu_a}{\mu_a}\right) W \tag{2.32}$$

where W is the weight of photon.

What follows in the procedure is the scattering of the photon. Deflection angle, $\theta\,(\theta \leq \theta \leq \pi)$, and an azimuth angle, $\psi\,(0 \leq \psi \leq 2\pi)$, are to be sampled statistically. We used the scattering function which has been defined by HG [80]. Since we are interested in media with scattering events having non-isotropic character, this option

seems reasonable, because it has been shown experimentally that Henyey-Greenstein function describes single scattering in media with anisotropy constant (shown as g) of about 0.9 [81]. The equation (2.33) below is used to compute the cosine of deflection angle:

$$\cos(\theta) = \begin{cases} \frac{1}{2g}\left[1 + g^2 - \left(\frac{1-g^2}{1-g+2g\xi}\right)^2\right] & , \quad g \neq 0 \\ 2\xi - 1 & , \quad g = 0 \end{cases} \tag{2.33}$$

where ξ is a random number.

The azimuth angle, however, is calculated by the equation below (2.34). ξ is a random number between 0 and 1.

$$\Psi = 2\pi\xi \tag{2.34}$$

The direction of propagation of the photon is updated by relations [47] below 2.35-2.37:

$$\mu_x' = \frac{\sin\theta\,(\mu_x\mu_y\cos\psi - \mu_y\sin\psi)}{\sqrt{1-\mu_z^2}} + \mu_x\cos\theta \tag{2.35}$$

$$\mu_y' = \frac{\sin\theta\,(\mu_y\mu_z\cos\psi - \mu_x\sin\psi)}{\sqrt{1-\mu_z^2}} + \mu_y\cos\theta \tag{2.36}$$

$$\mu_z' = -\sin\theta\cos\psi\sqrt{1-\mu_z^2} + \mu_x\cos\theta \tag{2.37}$$

However, in cases where the direction of the photon is close to the z-axis satisfying the criterion [56], $|\mu_z| > 0.99999$, formulas below 2.38-2.40 are used:

$$\mu'_x = \sin\theta\cos\psi \tag{2.38}$$

$$\mu'_y = \sin\theta\sin\psi \tag{2.39}$$

$$\mu'_z = SIGN\left(\mu_z\right)\cos\theta \tag{2.40}$$

where SIGN function returns 1 when is positive, -1 when is negative.

During its motion to next PMIS, photon can try to cross a boundary between the medium and ambient medium (top or bottom) or a boundary between two layers of the medium. Under these circumstances, a decision must be made whether the photon will cross the boundary or not. First of all, the angle of incidence, α_i , is calculated with the following formula 2.41:

$$\alpha_i = cos^{-1}\left(|\mu_z|\right) \tag{2.41}$$

Next Snell's law is used to find out critical angle of the boundary. Snell's law formulates the relationship between the angle incidence, the angle of transmission, and the reflective indices of the media that the photon comes from 2.42, n_i , and it goes to, α_t:

$$n_i \sin\alpha_i = n_t \sin\alpha_t \tag{2.42}$$

If the incidence angle is greater than critical angle, then the photon is reflected into the layer it comes from. Otherwise, internal reflectance is calculated using Fresnel Formula's [82] 2.43:

$$R(\alpha_i) = \frac{1}{2}\left[\frac{\sin^2(\alpha_i - \alpha_t)}{\sin^2(\alpha_i + \alpha_t)} + \frac{\tan^2(\alpha_i - \alpha_t)}{\tan^2(\alpha_i + \alpha_t)}\right] \tag{2.43}$$

To determine whether the photon is reflected or transmitted at the boundary, a random number is compared to internal reflectance. If the random number is greater than the internal reflectance, then the photon transmits. Otherwise, it is internally reflected [6].

When the photon is internally reflected, it completes the remaining step size of the previous sampling of it in the same layer it comes from. Before completing the step size, its directional cosines are updated as below Eq. 2.44:

$$(\mu_x, \mu_y, \mu_z) \longleftarrow (\mu_x, \mu_y, -\mu_z) \tag{2.44}$$

In case the photon transmits to the next layer of the slab, it continues its propagation with updated directional cosines and step size. New directional cosines are obtained by transforms, which are results of Snell's law (Eq. 2.45-2.47):

$$\mu_x' = \mu_x \frac{n_i}{n_t} \tag{2.45}$$

$$\mu_y' = \mu_y \frac{n_i}{n_t} \tag{2.46}$$

$$\mu_z' = \mu_z \frac{n_i}{n_t} \tag{2.47}$$

2.5.2 Differences of common MC Models

The MC simulation described above belongs to one of two major classes [81] [83]. The difference between these classes lies in the modeling of light tissue interactions. In

the first group [81] [83] photons are assumed to propagate in an absorbing substrate in which there are randomly distributed scattering centers. Even though scattering events are localized to scattering centers as it is in the second group, absorption is implemented differently than the second group. Photons are absorbed according to Eq. 2.48:

$$W_{remaining} = W_{initial} e^{-L_i \mu_a} \tag{2.48}$$

In this formula remaining weight of the photon packet loses in energy in a exponential manner when it completes a step. L_i represents the last step size traversed by the photon packet. Step size is also calculated with a different formula Eq. 2.49 Equation (2.30) according to this approach:

$$s = -\frac{\ln(\xi)}{\mu_s} \tag{2.49}$$

in which μ_t of Eq. 2.47 is replaced.

However, in the diffusion regime, they give close results.

2.5.3 Parallelization of the MC simulation

2.5.3.1 Random Number Generator. Even though MC simulation of light propagation is a reliable and strong tool, there is an important short coming inherent. To yield statistically reliable data by MC, the number of photon packets must be about hundreds of millions [84]. An empirical relation states the number of photons to get statistically significant data for source-detector range of 1 cm as Eq. 2.50:

$$N = \left[\left(\frac{\mu_a}{\mu_s'} \right)^{\frac{1}{2}} \right]^{\frac{1}{2}} \times 10^6 \tag{2.50}$$

Therefore, collecting reliable data by MC is directly proportional to number of photons simulated. To circumvent this speed problem MC simulations are parallelized [79] [80]. There is a subtle point which has to be considered carefully in paralleling the code. Random number generator (RNG) must be adjusted on each running computer such that the streams produced in each computer must guarantee that independent sampling is achieved on each node on the network. Therefore, RNG used is to be such that sub-streaming yields in enough sub-streams independent of each other. The RNG [85–87] have stream length of 2^{191} with 2^{76} sub-streams of 2^{127} sub-stream length which appropriate for sub-streaming.

3. MEAUREMENT SCHEMES IN NIR RELATED METHODS

3.1 General Aspects

In this work, particularly measurement schemes used for NIRs and DOI will be considered. In these applications tissue is usually probed by continuous-wave, frequency modulated and ultrashort (pico- or femto second range) light sources. (Figure 3.1). Probing of materials for non-invasive imaging (tomography) and spectroscopy could utilize various properties of light propagation like interference, diffraction and polarization. Hence, there are many optical techniques like optical coherence tomography, diffraction tomography, and applications of these to biomedical optics designed to use diffraction and coherence characteristics of back-scattered light [88–91]. Recently it has been reported that circular polarized light sustains its polarization properties much more than it does its directional properties. Utilization of polarization data leads to significant enhancement in optical imaging. Therefore, there is an increasing interest in measurement techniques besides the ones conventionally used for near-infrared spectroscopy (NIRs), functional near-infrared spectroscopy (fNIRS) and diffuse optical imaging (DOI) which are beyond scope of the current work.

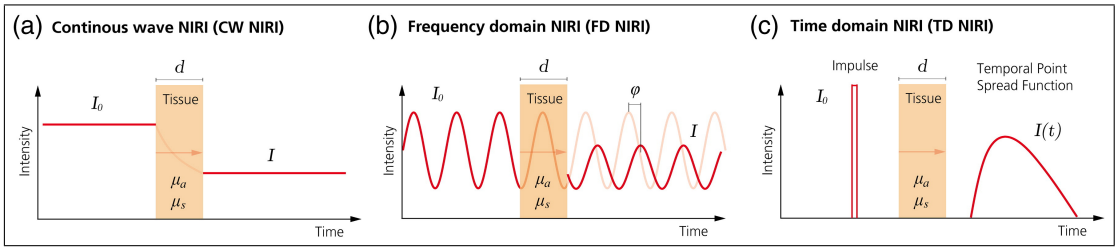

Figure 3.1 In continuous wave applications, the input intensity of NIR radiation is reduced inside tissue at the measurement side. For frequency domain applications, the applied light is driven in megahertz frequencies, whose decrease in intensity and phase change with respect to source modulation is measured. For time domain, a short pulse signal is introduced into the tissue, which is dispersed during its propagation inside the tissue. [92]

In medical in vivo studies, researchers generally examine cases in two different geometries: semi-infinite and slab. For the semi-infinite geometry, the only available

measurement is diffuse reflected wave, whereas for the slab geometry both transmitted and diffuse reflected can be obtained (Figure 3.2).

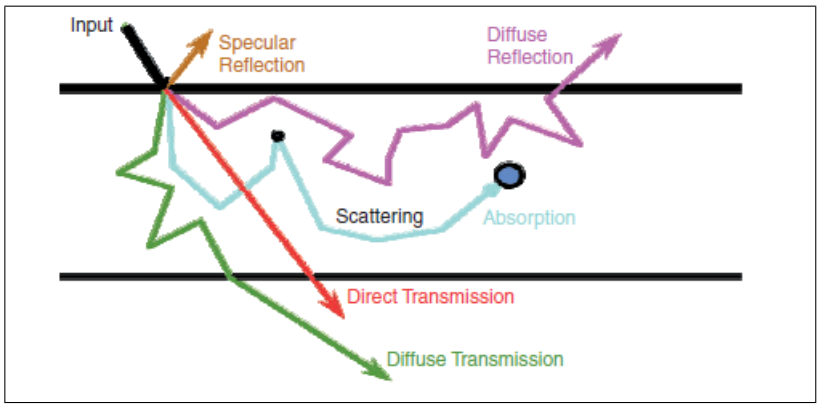

Figure 3.2 Possible scenarios for photon propagation in a slab. Slab can reflect the photon in a specular way, reflect diffusely, absorb, direct transmittance or diffuse transmittance [93].

3.2 Intrinsic biomedical contrast and related measurements

The main idea of optical spectroscopy and tomography is the detection of NIR photons interacting with tissue while traversing tissue. Thus, understanding the mechanisms which result in biomedical contrast is of substantial importance. The ways of interactions of NIR light for intrinsic biomedical contrast are only scattering and absorption. In Figure 3.3, the absorption coefficients of different tissue constituents with respect to the wavelength of incident radiation are given

Function associated temporal variations of scattering properties of tissues in living systems are seen in excitable cells [94–96]. The main mechanism behind this is the change in neuron structure during action potential propagation and synaptic transmission [94]. Experimental data on isolated axons (Figure 3.4) elucidated that action potential has an effect on scattering properties of the axon [94] [97]. A series of experiments conducted resulted that currents through axon membrane during action potential lead to an increase in KCI concentration in the 100 A° between axonal and Schwann cell membranes. This concentration change establishes an osmotic pressure gradient that would result in volume changes [94]. This change occurs in the same time

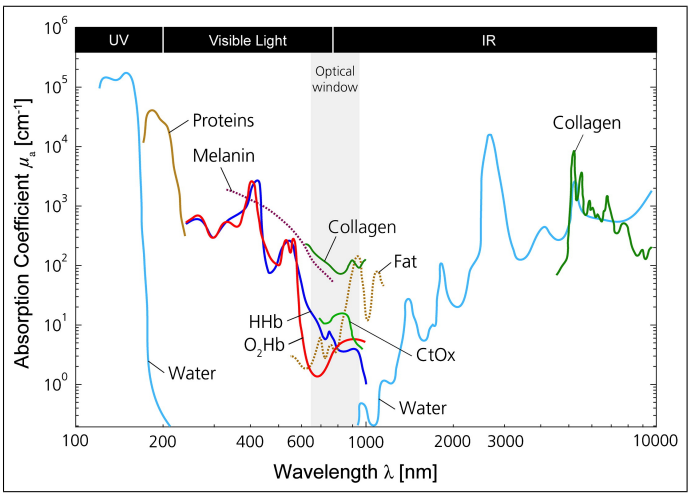

Figure 3.3 Absorption coefficients of main tissue constituents. [92]

of action potential [94], and measured in the order of hundreds of milliseconds [94] [97]. It is believed that this mechanism results in a detectable signal which is a result of cumulative response of the brain tissue active almost synchronously. A huge number of cells are activated during a task or stimulus and cellular membranes have refractive indices different from the refractive indices of the intracellular and extracellular space, leading to light scattering [98].

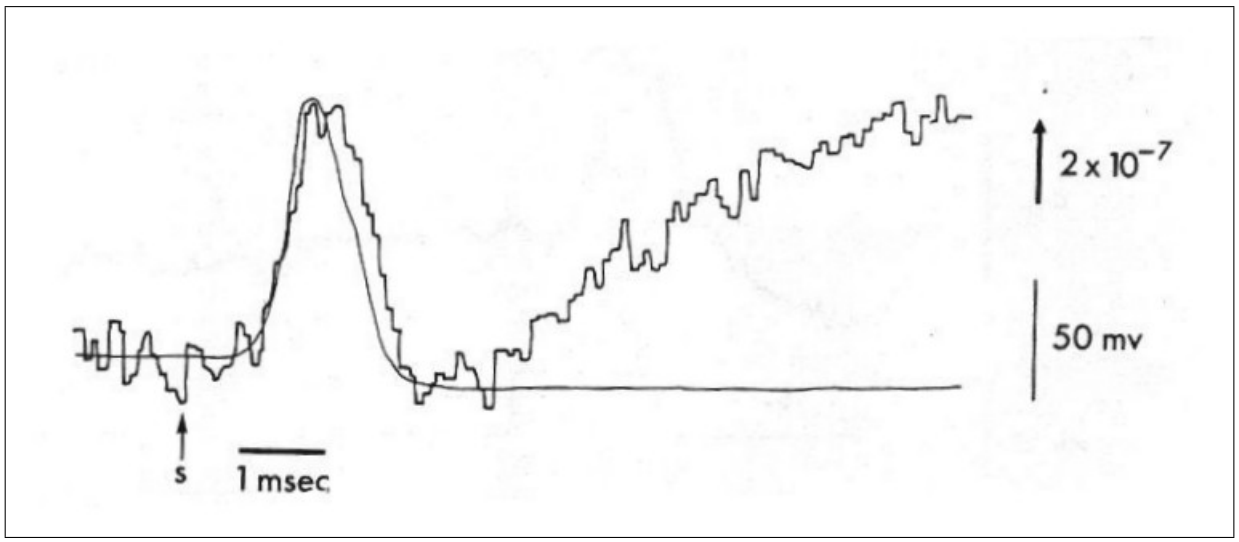

Figure 3.4 Light scattering pattern (zig-zag, heavy line) measured from L. forbesi during action potential (thin line). Light scattering has two phases, one is accompanying the spike and the other a slow, long lasting increase continuing long after the action potential [94].

Absorption properties in living tissue of NIR can change due to presence of NIR-

specific chromophores. Chromophore is a substance whose absorbance is high for a particular wavelength. For NIR light, (Figure 3.3) the absorbance of tissue components is relatively low, which enables penetration of NIR photons into a living tissue for several centimeters. Significant choromophores of NIR light is deoxy-hemoglobin (HBR), hemoglobin (HbO_2) and cytochrome oxidase (CtO_x) [99]. Further, these chromophores have oxygenenated and deoxygenated forms, with different absorption spectra [100]. Since the major chromophores of NIR photons are not present in bone structure, it is possible to collect data through human skull.

Measurement of relatively fast change of scattering properties of the neurons following the neuronal activity, have been utilized in various and numerous biomedical studies [98] [101]. In addition to this change in scattering properties, neuronal activity leads to a change in absorption characteristics of the surrounding vascular tissue. Since NIR radiation is subject to certain chromophores such as oxygenetated hemoglobin (HbO_2), de-oxygenetad hemoglobin (HbR) and cytochrome oxidase, it is potentially possible to measure and quantify brain activity through skull and scalp. NIR radiation penetrates human tissues, since the dominant factor in its tissue transport is scattering, which is typically about 100 times more probable than absorption [102] and the relatively high attenuation of NIR light in tissue is due to the main chromophore hemoglobin (the oxygen transport red blood cell protein) located in small vessels (< 1 mm in diameter) of the microcirculation, such as capillary, arteriolar and venular beds. NIRS is weakly sensitive to larger blood vessels (> 1 mm) because they completely absorb the light. Since there is the fact that arterial blood volume fraction is about 30% in human brain [103], the NIRS technique offers the possibility to obtain information mainly concerning oxygenation changes occurring within the venous compartment. Hence, there are three intrinsic biomedical contrast mechanisms for the brain activity:

a) Neural activation: Fast optical signal, with delay of about 1-10 ms after the onset of the experimental task/stimulus can be measured due to the change in scattering properties of brain during activation

b) Metabolic activation: Metabolic response with a delay about 500-100 ms

after the onset of the task/stimulus, due to the activity of CtO_x.

c) Neurovascular activation (or cerebral hemodynamic response): Slow optical signal, with a delay of about 2-5 sec, due to the change of local concentrations of HbO_2 and HbR [98].

Depending on this feature of NIR radiation, many studies have shown the applicability of NIR dependent instruments to obtain data related to brain activity in intact brain, non-invasively and non-destructively. In most NIR related application the change in concentrations of [HbR], [HbO_2], [CtO_x] and their derived relations are of medical significance [42] [101] [104–113]. The most vital derived relations in this fields are:

Blood volume:

$$[BV] = [HbR] + [HbO_2] \tag{3.1}$$

And the relative saturation:

$$[StO_2] = \frac{[HbO_2]}{[HbO_2] + [HbR]} \tag{3.2}$$

whose values give a measure of anoxic and hypoxic state of a region in a certain location inside a tissue [114].

Cytochrome oxidase is an enzyme, which is present in all eukaryotes, and forms parts of the cell membrane in some prokaryotes [99]. It is a transmembrane protein of inner mitochondrial membrane whose main function as the terminal enzyme in electron transport chain is to catalyze the transfer of electrons from its reduced substrate ferrocytochrome c to molecular oxygen to form water [99]. One of the important aspect of this reaction is the generation of ATP by the coupled process of oxidative phosphorylation.

Excitable cells should remain excitable to maintain their excitability through

active transport. Hence, the human brain which is composed of enormous number of excitable neurons, corresponding to only 2% of the total body weight, consumes at least 20% of the total oxygen intake by the body at rest. The human brain derives most of its energy from aerobic metabolism, specifically of glucose. ATP is consumed for active ion pumping to sustain the resting membrane potential, fast axoplasmic transport and the synthesis of macromolecules and neurotransmitters. Of these, the upkeep ion balance is the major energy consuming function of neurons. In Figure 3.5, the function of CtOx related to neuronal activity is shown.

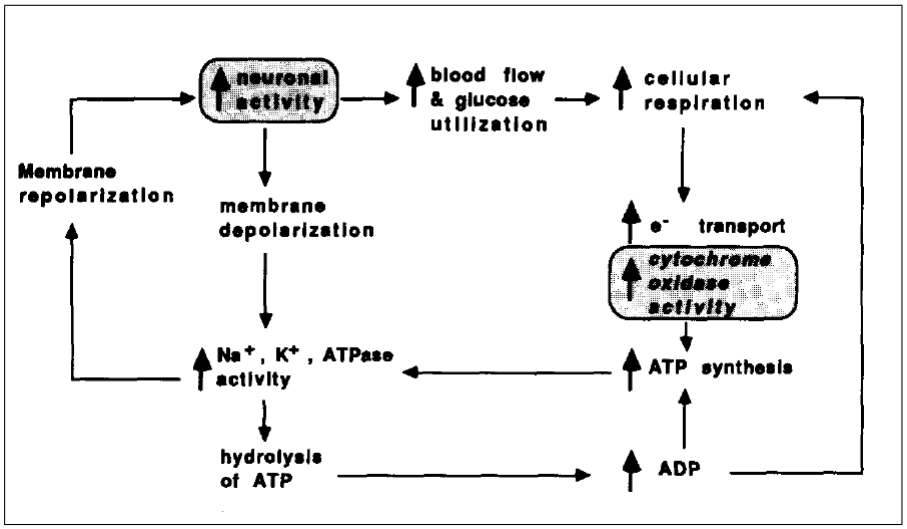

Figure 3.5 The function of cytochrome oxidase related to neuronal activity is shown [99].

Hence the ability of measurement of the concentration and oxidation state of cytochrome oxidase is of high value in medicine and science. The temporal resolution is about 1 ms. [101].

Furthermore, to these relatively fast intrinsic contrast mechanisms, there is a long-duration contrast mechanism which could arise by the formation of new blood vessels (angiogenesis) during the progression of a tumor or during development. Therefore, the detection and monitoring of angiogenesis in a repeated, non-invasive, non-hazardous manner is of quite high medical value. The relation between angiogenesis and tumor growth for different types of tumors have been shown in the literature [115–117] in addition to other non-invasive optical monitoring techniques [118]. Techniques have been developed for tumor monitoring by the assessment of state of angiogenesis raised

by converting blood volume measurement obtained by NIRS [119] [120]. Specifically, it has been shown that cerebral blood volume measured by NIRS could be utilized as marker of angiogenesis [120]. The detection, location and identification of tumor embedded inside the tissue is one of the ultimate goals in DOI, which is to reconstruct 3D of a region-of-interest, since tumor has elevated values of absorption and scattering properties with respect to surrounding tissue due to angiogenesis.

3.3 Extrinsic Biomedical contrast

The use of exogenous agents administered inside the body is the ultimate contrast type. The main idea behind the exogenous agent is to increase the intrinsic contrast of a target such as a tumor. This goal can be achieved by increasing absorption and scattering properties of the target. The available NIR exogenous contrast agent is indocyanine green (ICG) [121] whose extinction coefficient is high. This agent provides vascular bed volume and extravagates readily in tumors [95].

4. METHODS

4.1 The solution of photon migration in the presence a single defect

An optical defect (absorber) residing in a turbid medium introduces a perturbation to NIR light propagation that is represented as decrease in measured response. Physically the perturbation is a function of the distance between the defect and the detector when the source and the detector positions are fixed. For a configuration of a single source and multiple detectors in a row (Figure 4.1), the perturbation will be less at the farther detectors as long as the defect resides between the source and the closest detector. We propose a method to extract the depth information from the differential effect of perturbation on multiple detectors in a row.

In this study, a solution of time-independent diffusion equation of photon propagation in turbid media is used for simulations [122]. This solution is derived for the case where the semi-infinite medium is illuminated by a CW source.

The response of a medium containing a spherical in-homogeneity is referred as the perturbed response (literally total photon-flux-density (J_T) in units of detected photons per unit area per unit time at the measurement site).J_T is the summation of two components J_0 and J_1, the response of the unperturbed background medium and the perturbation introduced by a spherical defect respectively [122].

$$J_0 = \delta \left| \vec{E}_0 (\vec{r}) \right| \tag{4.1}$$

where $\vec{r}$ is radius vector to the point of interest (in Cartesian coordinates x, y, z) and $\vec{E}_0 (\vec{r})$ (in units of photons per unit time per unit volume) is [122]:

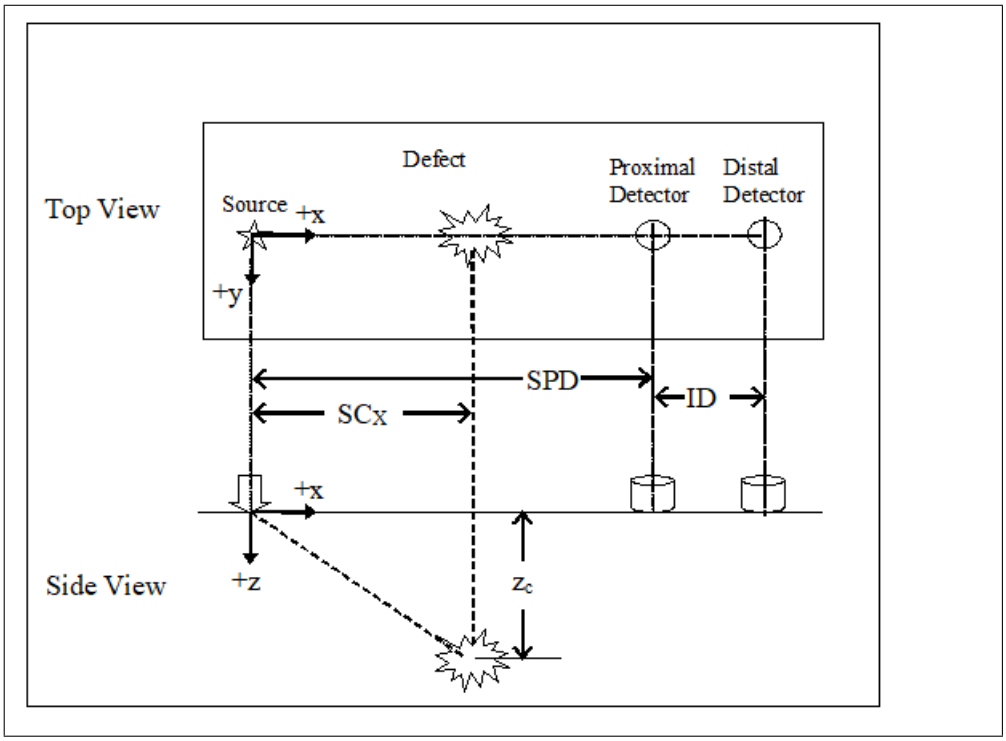

Figure 4.1 The method consists of a CW source (S) and the measurement of diffuse reflectance at two distances. The source, proximal and the distal detectors are located on a row (y=0). The defect resides between the source and the proximal detector. SPD: source-proximal detector distance; ID: inter-detector distance; SCX: x component of source-center of the defect distance. The origin of Cartesian coordinate system is the location of the source and +x, +y and +z are as shown.

$$\vec{E}_0(\vec{r}) = \frac{z_0 S_0}{2\pi\delta}\left(\frac{3\kappa z\vec{r}}{r^4} + \frac{3z\vec{r}}{r^5} - \frac{\kappa\hat{z}}{r^2} - \frac{\hat{z}}{r^3} + \frac{\kappa^2 z\vec{r}}{r^3}\right)e^{-\kappa r} \tag{4.2}$$

where δ is the diffusion coefficient which equals $\frac{1}{3[\mu_a+\mu_s']}$ (in unit of length, μ_a and μ_s' are absorption and transport scattering coefficients of the medium respectively), $\kappa = (\mu_a/\delta)^{\frac{1}{2}}$ (in unit of $[L^{-1}]$), z_0 is the extrapolation depth $\left(\frac{0.7}{\mu_s'}\right)$, r is the magnitude of radius vector ($\vec{r}$) and S_0 (in units of photons per unit time) is the photon injection rate which is constant in CW cases.

The perturbation by the spherical defect at the detector site (J_1) is:

$$J_1 = 2\delta q \frac{(\kappa |\vec{r}_c - \vec{r}_d| + 1) z_c}{|\vec{r}_c - \vec{r}_d|^3} \exp(-\kappa |\vec{r}_c - \vec{r}_d|) \phi_0(\vec{r}_c)$$
$$- 2\delta p \left\{ \frac{\left[(\vec{r}_c - \vec{r}_d) \cdot \vec{E}_0(\vec{r}_c) \right] (\kappa |\vec{r}_c - \vec{r}_d| + 3) z_c}{|\vec{r}_c - \vec{r}_d|^5} - \frac{E_0(\vec{r}_c)}{|\vec{r}_c - \vec{r}_d|^3} \right\} \exp(-\kappa |\vec{r}_c - \vec{r}_d|) \quad (4.3)$$

where $\vec{r}_c$ is the radius vector of the center of the defect with Cartesian coordinates (x_c, y_c and z_c), $\vec{r}_d$ is the radius vector of the detector with Cartesian coordinates. The multiplicands q (in units of length) and p (in units of volume) are functions of optical properties of the defect ($\tilde{\mu}_a$ *and* $\tilde{\mu}'_s$), optical properties of the medium (μ_a *and* μ'_s) and the radius of the defect [122]. The $\phi_0(\vec{r}_c)$ (in units of photons per unit area per unit time) is the photon fluence-density-function at the center of the defect [122].

Some of the properties of the multiplicands q and p are to be stressed. When $\tilde{\mu}_a = \mu_a$, q is zero. On the other hand, such a relation does not exist for p when $\tilde{\mu}_s = \mu_s$. It has been reported that an absorber embedded in a semi-infinite medium modifies CW diffuse reflectance such that, a shadow on the measurement surface appears [42]. Methods depending on this idea have been shown to detect the projection of a single defect or two defects onto the measurement surface for the semi-infinite geometry; at the expense of multiple measurements with spatially resolved sampling.

4.2 General Approach

4.2.1 Generation of Ratio-vs.-Depth Curve

As it was reported by Feng et.al., if q is non-zero (for $\mu_a \neq \tilde{\mu}_a$) in Eq. 4.3, the term with multiplicand q is dominant in practice [122]. When the Eq. 4.3 is truncated as:

$$J_1 \approx 2\delta q \frac{(\kappa\,|\vec{r}_c - \vec{r}_d| + 1)\, z_c}{|\vec{r}_c - \vec{r}_d|^3} \exp\left(-\kappa\,|\vec{r}_c - \vec{r}_d|\right) \phi_0\left(\vec{r}_c\right) \tag{4.4}$$

for a fixed source, the ratio of two values of J_1's calculated for two different detector distances (Figure 4.1) is

$$\frac{J_1^P}{J_1^D} = \frac{2\delta q \frac{\left(\kappa\left|\vec{r}_c - \vec{r}_d^{\,P}\right| + 1\right) z_c}{\left|\vec{r}_c - \vec{r}_d^{\,P}\right|^3} \exp\left(-\kappa\left|\vec{r}_c - \vec{r}_d^{\,P}\right|\right) \phi_0\left(\vec{r}_c\right)}{2\delta q \frac{\left(\kappa\left|\vec{r}_c - \vec{r}_d^{\,D}\right| + 1\right) z_c}{\left|\vec{r}_c - \vec{r}_d^{\,D}\right|^3} \exp\left(-\kappa\,|\vec{r}_c - \vec{r}_d^{\,D}|\right) \phi_0\left(\vec{r}_c\right)} \tag{4.5}$$

where superscript P is for proximal and superscript D is for distal. Since q, δ and $\phi_0\left(\vec{r}_c\right)$ are equal for both the numerator and denominator, they cancel out and Eq. 4.5 becomes:

$$\frac{J_1^P}{J_1^D} = \frac{\frac{\left(\kappa\left|\vec{r}_c - \vec{r}_d^{\,P}\right| + 1\right)}{\left|\vec{r}_c - \vec{r}_d^{\,P}\right|^3} \exp\left(-\kappa\left|\vec{r}_c - \vec{r}_d^{\,P}\right|\right)}{\frac{\left(\kappa\left|\vec{r}_c - \vec{r}_d^{\,D}\right| + 1\right)}{\left|\vec{r}_c - \vec{r}_d^{\,D}\right|^3} \exp\left(-\kappa\,|\vec{r}_c - \vec{r}_d^{\,D}|\right)} \tag{4.6}$$

Since the placement of detectors can be arranged, the components of detector vectors ($\vec{r}_d^{\,P}$ and $\vec{r}_d^{\,D}$) are fully known. Operands of κ (μ_a and μ_s') can be assessed by optical methods in vivo [123–127]. Please note that zc in Eq. 4.5 cancel out in Eq. 4.6. The depth information of the center of the defect remains as a Cartesian component of $\vec{r}_c$ with respect to origin x_c, y_c and z_c. Assuming that the planar coordinates (x_c and y_c) of the defect relative to the source are known [127], depth (z_c) remains the only unknown independent variable on the right hand side of the Eq. 4.6 implicit in $\vec{r}_c$. A curve generated by Eq. 4.6 for a range of z_c (typically from 5.0 mm to 40.0 mm) is referred as the Ratio-vs.-Depth curve throughout the text. The generation of

Ratio-vs.-Depth curve does not include the knowledge of absorption coefficient of the defect ($\tilde{\mu}'_a$) and radius of the defect (a).

In this study, for all cases, the location of proximal detector with respect to source is arranged such that the defect always resides between the source and the proximal detector. Both the source and detectors are taken as extended source and detectors of 1 mm^2 core-area to have a realistic calculation.

4.2.2 Depth Estimation

Optically turbid medium is considered to contain an absorbing spherical defect whose scattering coefficient is the same as the medium (Figure 4.1). The ratio of *perturbed responses of the medium* measured at the proximal and distal detectors is:

$$R = \frac{\left(J_0^P + J_1^P\right)}{\left(J_0^D + J_1^D\right)} \tag{4.7}$$

For the same source-detector pairs the unperturbed response of the background medium (J_0) can be calculated (Eq. 4.1) using optical parameters (μ_a and μ'_s) that are already obtained from look-up tables [5] or measured experimentally [123–129]. Then J_0's of proximal and distal detectors are subtracted in numerator and denominator of Eq. 4.8 respectively:

$$R = \frac{\left(J_0^P + J_1^P\right) - J_1^P}{\left(J_0^D + J_1^D\right) - J_1^D} \tag{4.8}$$

When R is matched with its corresponding value in the y-axis of Ratio-vs.-Depth curve, the depth is estimated from the x-axis. The Ratio-vs.-Depth curve is generated by Eq.

4.6 with the same optical parameters used for the calculation of J_0 and with the same relative placement of detectors with respect to source and the defect (Figure 4.2).

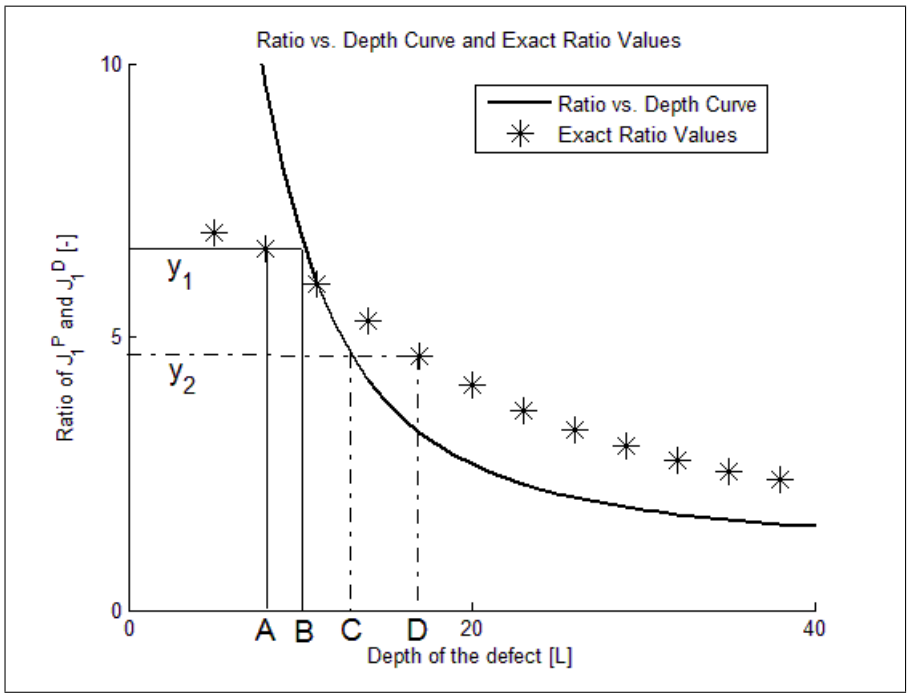

Figure 4.2 Schematic view for the depth estimation and error calculation. The solid line corresponds to Ratio-vs.-Depth curve, which is generated by Eq. 4.6. Stars on the graph show exact ratio values (rarefied for clearance) obtained by Eq. 4.3 with the same parameters and the set of depth values. For the exact depth A first, y1 is calculated and y1 is projected into horizontal axis to B via the Ratio-vs.-Depth Curve. Hence, the error at depth A is the absolute value of A-B divided by the diameter of the defect. For the depth C, the error is the absolute value of C-D divided by the diameter of the defect.

Knowledge on the unperturbed response is required for the application of the proposed method. The method is further extended (described in part III.4) for the cases where the unperturbed response might be erroneously calculated.

4.2.3 Analysis of the proposed method

The distance from the source to the planar location of the defect (SC_x), source-proximal-detector distance (SPD) and inter-detector distance (ID) can be adjusted according to physical conditions (Figure 4.1). Absorption coefficient and radius of the defect (a) do not take part in the generation of Ratio-vs.-Depth curves (Eq. 4.6), but still can influence the results since they are present in Eq.4.3 in p and q. Therefore, the

analysis of the method comprises two approaches. First the effect of placement of source and detectors on *Ratio-vs.-Depth curves*, second the precision of the depth estimation under different probe placement for different defect size and defect/background medium absorption coefficient are analyzed.

The geometry used to derive Ratio-vs.-Depth Curves is shown in Figure 4.1.

Even if the defect is a pure absorber ($\mu_s' = \tilde{\mu}_s'$), the frequency of scattering events inside the defect are increased compared to the background. This could be attributed to light-tissue interaction results from simultaneous scattering and absorption [60]. The precision of the method is tested quantitatively by calculating error introduced by the approximation (setting p=0 in Eq. 4.2). The error is defined as follows: for a particular depth of the center of defect (e.g. point A in Figure 4.2), the exact ratio (y_1) is calculated by exact formula (Eq. 4.2) and plotted as the point (A, y_1) in Figure 4.2. Ratio-vs.-Depth Curve (by Eq. 4.6) obtained by the same geometry and optical properties is plotted on the same graph. The exact ratio (y_1) is projected onto the depth axis to obtain assessed depth via the Ratio-vs.-Depth Curve (point B in Figure 4.2 Hence the error at depth A is obtained by dividing the absolute value of the difference between A and B with the diameter of the defect. The divisor is chosen as the diameter of the defect to compare cases with different defect sizes and to avoid depth dependence on the error.

For the quantitative analysis of the method the errors are calculated for different sets of ID, SC_x, z_c, background medium and defect optical parameters (Figure 32). Additionally, we studied the error introduced due to possible mistakes in lateral coordinates (Figure 33). Errors are shown with filled-contour matrices as a function of z_c and SC_x (Figure 32 and Figure 33).

4.2.4 Analysis of Probable Errors in Experimental Conditions

The necessity to calculate the response of the background (J_0) might be a limiting factor in the applicability of our method for cases where the relatively accurate knowledge on the background optical properties is not available either experimentally or from the literature. A set of optical parameters (predicted from the literature) can be used in iterative algorithms. One approach to use for iterations might be to measure the response of the probed medium with an array of detectors for a configuration in which the defect does not reside between the source and detectors.

The erroneous prediction or estimation of the medium optical parameters is studied, and extension of the method is suggested for improved depth assessment. To analyze this case, the measured response is simulated by feeding a set of optical parameters (actual μ_a and μ_s') to Eq. 4.3. Then unperturbed response of the medium (J_0) is calculated for a range of μ_a and μ_s' selected around the ?actual? values and a matrix of calculated ratio values is obtained. The physical constraints require two conditions to be satisfied. First, for each detector (both proximal and distal) the measured response must be less than the corresponding calculated J_0. Second, the effect of perturbation must be greater at the proximal detector compared to the distal one (ratio values greater than one). The upper limit of the calculated J_0 was set not to be higher than three folds of the measured response physically [123][122]. The first step is to exclude the set of parameters with non-physical outcome from the matrix. The candidate set of optical parameters is then used to estimate the depth of the defect from the corresponding Ratio-vs.-Depth curves for spatially resolved measurements. The next step is to compare the depth values within matrices obtained from different measurements. The depth estimation with smallest standard deviation for the assessed depth values is taken to correspond to the one obtained with the optical values closest to the actual ones (Figure 5.6).

4.2.5 Experimental Material and Experimental Procedure

An aquarium with darkened sides with dimensions $100.0x100.0x100.0\ mm$ is filled with 1% intralipid. The aquarium is made of PVC and the top of the aquarium is drilled to hold the 1.1 mm core diameter (whose area taken as 1.0 mm^2) fibers as sources and detectors. A 1 kHz frequency signal is used to operate a 3 mW, 785 nm diode laser (RLD78MA-E Thorlabs). Lock-In Amplifier is used to lock the signal to the chosen frequency and eliminate the noise (SRS SR510 Stanford Research). The optical properties of the intralipid solution used in the experiment are $\mu_a = 0.002mm^{-1}$ and $\mu_s' = 0.827mm^{-1}$ by measurement. A 1.0 cm^3 dark gray cubical rubber is placed at the symmetrical center between source and detector fibers. The source-proximal detector distance is 20.0 mm and the inter-detector distance is 10.0 mm to avoid the effect of field-of-view (FOV) of detectors on measurements [130] [131] [132][130]-[132]. The source-center of the defect distance is 10.0 mm. Diffuse reflectance values are obtained via descending the rubber by a step size of 1 mm starting at 15 mm to 40 mm (with respect to the center of the rubber from the sample-ambient layer boundary). The depth range chosen enabled to make measurements of enough intensity. The J_0 is obtained by measuring spatially-resolved reflectance after the cube is removed from the aquarium.

5. RESULTS

5.1 Simulation Results

The diffusely reflected photons injected into a semi-infinite turbid medium by a CW source, traverses the medium in the shape of banana to reach a detector [133]. The banana SSP profile moves towards the medium-air interface with a sharper peak and narrower distribution [134] when the absorption coefficient of the medium increases. Since the volume of the defect is small with respect to volume probed, the banana shaped SSP will be used qualitatively in this study.

The optical parameters used in this study are selected to resemble typical in vivo parameters for biological tissue cited in literature [5]. Absorption contrast between the defect and the background medium is four fold in accordance to previous studies [135].

The relative placement of detectors and the source with respect to planar position of the defect is an important parameter since different combinations yield different *Ratio-vs.-Depth curves* (Figures 5.1-5.3). The effects of different values for SC_x, ID, SPD are studied in this work (Table 5.1).

Table 5.1
Parameters used for curve generation in Figures 5.1-5.3

	SC_x [mm]	SPD [mm]	ID [mm]	a [mm]	μ_a [mm^{-1}]	$\tilde{\mu}_a$ [mm^{-1}]	μ_s' [mm^{-1}]	$\tilde{\mu}_s'$ [mm^{-1}]
Fig. 5.1	0.0/5.0/10.0 15.0/20.0	20.0	2.5	3.5	0.005	0.02	2.0	2.0
Fig. 5.2	0.0	10.0/20.0 30.0	2.5	3.5	0.005	0.02	2.0	2.0
Fig. 5.3	0.0	20.0	2.5/5.0 7.5/10.0	3.5	0.005	0.02	2.0	2.0

Ratio-vs.-Depth curves are generated (Eq. 4.6) for a range of defect depth from 1 mm to 30 mm with a step size of 1 mm. (Figures 5.1-5.3). To visualize the effect of the neglected term, ratio values obtained by the exact relation given in Eq. 4.3 are displayed in the same figures (Figures 5.1-5.3) Used optical and geometrical parameters are displayed in Table 5.1. For each set of parameters, depths of the center of the defect are taken from 4 mm to 30 mm with a step size of 2 mm (14 values in Figures 5.1-5.3).

In a fixed constellation of source relative to the detectors (constant SPD and ID) it is possible to construct Ratio-vs.-Depth curves with different characteristics via changing the placement of source relative to the planar position of the defect (Figure 5.1).

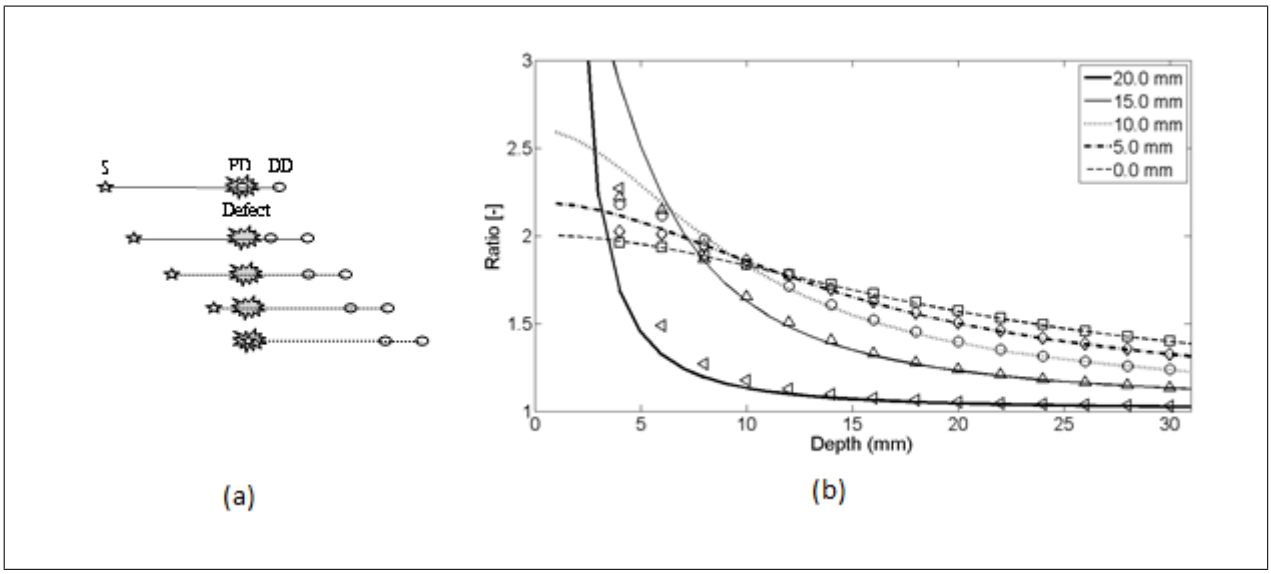

Figure 5.1 Ratio-vs.-Depth curves generated for different source-center of the defect distance (SC_x). Five distances are used: 0.0, 5.0, 10.0, 15.0 and 20.0 mm. (a) Top views of simulated geometries are depicted. S: Source, PD: proximal detector, DD: distal detector. Irregular gray shape symbolizes the defect. From top to bottom, SC_x= 20.0, 15.0, 10.0, 5.0 and 0.0 mm. (b) The effect of SC_x on Ratio-vs.-Depth curves and exact values are displayed , where Dashed curve / Circle (SC_x = 0.0 mm), dash-dot / diamond (SC_x = 5.0 mm), dotted / cross (SC_x = 10.0 mm), thin-solid / triangle-ups (SC_x = 15.0 mm) and thick-solid / triangle-downs (SC_x = 20.0 mm). SPD = 20.0 mm; ID = 2.5 mm.

As SC_x approaches SPD, the perturbation at the proximal detector increases resulting in Ratio-vs.-Depth curves starting at higher ratio values. When proximal detector is located close to the defect, scattering effect of the defect is more pronounced and the discrepancy between Ratio-vs.-Depth curves and exact values generated by Eq.

4.3 become evident for defect depths less than 10 mm. For all cases, as the defect is deeper than 10.0 mm, the discrepancy between *Ratio-vs.-Depth curves* and exact ratio values diminish due to longer distance to detectors.

The modification introduced in *Ratio-vs.-Depth curve* for different values of SPD is given in Figure 5.2. The defect is directly below the source for all cases (SC_x = 0.0 mm). The Ratio-vs.-Depth curves and exact values overlap quite well for all depths. The discrepancy at depths less than 10.0 mm seems to increase, as SPD gets shorter. A possible explanation would be the augmentation of scattering effect of the defect.

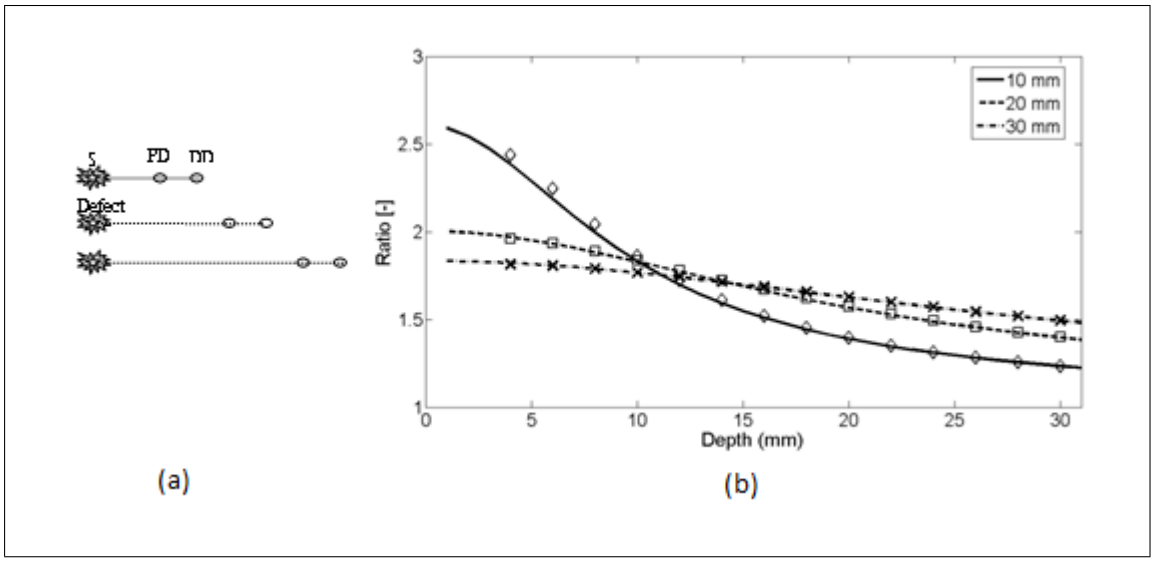

Figure 5.2 The effect of source-proximal detector distance (SPD) on Ratio-vs.-Depth curves. When the PD is placed relatively farther, the perturbations in detectors become close to each to other. (a) Top views of simulated geometries are displayed. Irregular gray shape symbolizes defect, S is the source, PD and DD are proximal and distal detectors respectively. For the two geometries in bottom, labels are not drawn. From top to bottom: SPD = 10.0, 20.0 and 30.0 mm. Inter-detector distance (ID) = 2.5 mm and the source is directly placed above the defect. (b) Ratio-vs.-Depth curves and exact ratio values are displayed: Dash-dot curve/ cross (SPD = 30.0 mm), dashed curve / triangle-ups (SPD = 20.0 mm), solid curve/ triangle-downs (SPD = 10.0 mm). SC_x = 0.0 mm; ID = 2.5 mm.

Results for four different values of inter-detector distance (ID) are shown in Figure 5.3. As the ID gets longer, Ratio-vs.-Depth curve starts at higher values because of the decrement of interference of the defect in the detected light intensity of the distal detector. There are minute discrepancies between exact values and Ratio-vs.-Depth curves for all situations that are given.

For the analysis of errors in depth estimation (Figure 4.2), the defect is consid-

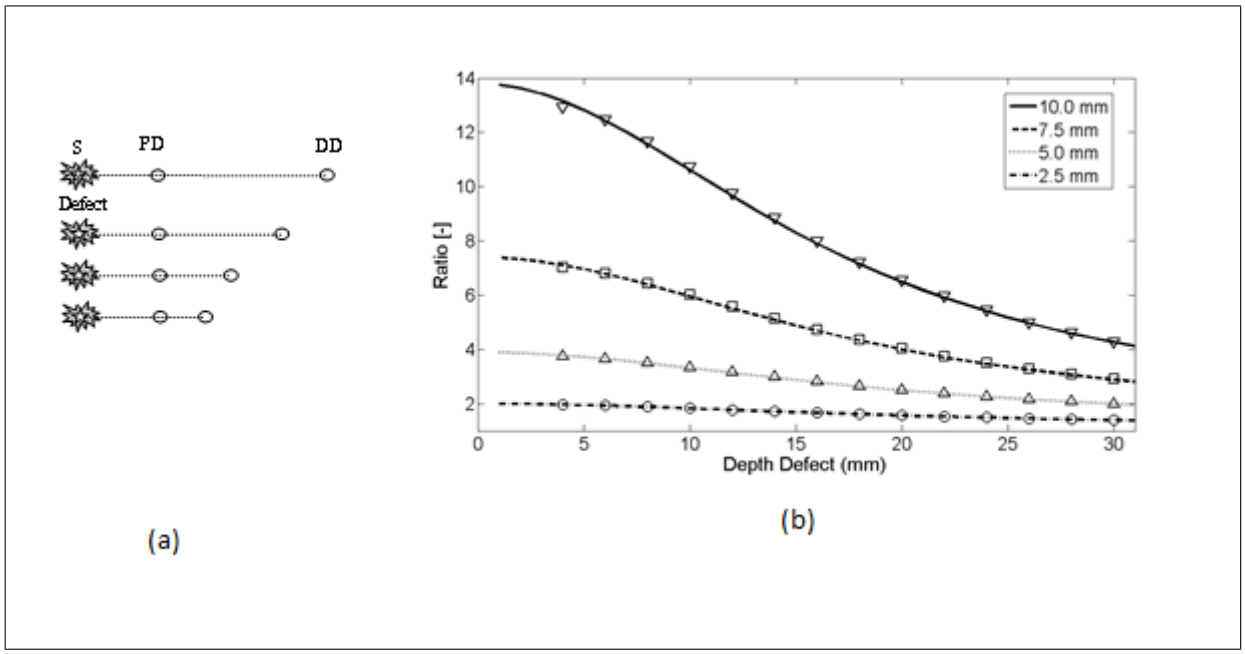

Figure 5.3 *Ratio-vs.-Depth curves* for different inter-detector distances (ID). As expected, when the distance between proximal detector (PD) and distal detector (DD) is longer, the perturbation measured at PD becomes more than that at DD. (a) Four different cases depicted in top views of geometries, from top to bottom, ID = 10.0, 7.5 , 5.0 and 2.5 mm respectively. S show the source, PD is the proximal and DD is distal detector. Irregular gray shape symbolizes the defect in all cases. (b) The Ratio-vs.-Depth curves and exact ratio values are displayed: dash-dot curve / circle (ID = 2.5 mm), dotted curve/ triangle-ups (ID = 5.0 mm), dashed curve / cross (ID = 7.5 mm), solid curve / triangle-down (ID = 10.0 mm). SC_x = 0.0 mm; SPD = 20.0 mm. For the SPD of 20.0 mm, *Ratio-vs.-Depth curve* match better with exact values

ered to take evenly distributed positions in the region of interest (ROI). ROI is the vertical plane (y = 0.0) that spans the distance between the source and the proximal detector in +x direction (0.0 mm $\leq$ x $\leq$ SPD) and a range for defect depth values in +z direction (ceiling (the radius of the defect) mm + 2.0 mm) $\leq$ z $\leq$ 40.0 mm). In Fig. 32a-d, the defect takes 21 evenly spaced locations in +x direction. In Figure 5.4a,5.4b and 5.4d the defect are assumed to locate at 37 locations in +z direction spanning from 4.0 mm to 40.0 mm with a step size of 1.0 mm. For Figure 5.4c, however, z_c spans from 7.0 mm to 40.0 mm with 34 depth locations. Optical and geometrical parameters used for error maps are given in Table 5.2.

In Figure 5.4a error is less than 2.5% of the diameter of the defect when the depth of the center of the defect is below 10.0 mm and its distance from the source is

Table 5.2
Parameters used for error calculation in Figures 5.4(a-d), 5.5(a-d) and 5.6.

	SPD [mm]	ID [mm]	a [mm]	μ_a [mm^{-1}]	$\tilde{\mu}_a$ [mm^{-1}]	μ'_s [mm^{-1}]	$\tilde{\mu}'_s$ [mm^{-1}]
Fig. 5.4a-5.5a	30.0	2.5	2.0	0.005	0.02	2.0	2.0
Fig. 5.4b-5.5b	30.0	**10.0**	2.0	0.005	0.02	2.0	2.0
Fig. 5.4c-5.5c	30.0	2.5	**5.0**	0.005	0.02	2.0	2.0
Fig. 5.4d-5.5d-5.6	30.0	2.5	2.0	**0.050**	**0.20**	2.0	2.0

less than 23 mm. The maximum value of error is greater than 15%, which is constrained to a very narrow band at 4.0 mm $<$ z $<$ 5.0 mm and 2 mm $<$ x $<$ 12 mm.

When ID is extended (from 2.5 mm to 10.0 mm) the banana of the distal detector becomes more spread (Figure 5.4a compared to Figure 5.4b). Therefore, the superficial region of the medium is less equally populated with bananas of proximal and distal detectors resulting in a slightly more extended error in the superficial region. Bigger defect causes (Figure 5.4c) errors in the range of 15% when it is in the superficial region (7.0 mm $<$ z_c $<$ 8.0 mm and 5 mm $<$ SC_x $<$ 23 mm). Increase in the absorption coefficient of the medium shifts bananas of both detectors towards the surface (with a sharper peak and narrower distribution [134]. Hence the superficial region becomes more equally populated by the photons of proximal and distal detectors resulting in a decreased error (Figure 5.4d compared to Figure 5.4a).

In general, for all cases the error is smallest when the source is placed close to the defect ($SC_x$$<$SPD/2). Photons reaching the two detectors do not equally populate the vertical region below the proximal detector (SC_x $\sim$SPD) resulting in a higher error in the depth estimation. Increasing ID (Figure 5.4b) widens the banana of the distal detector and decreases error. Bigger defects (Figure 5.4c) might increase errors when the proximal detector is placed above or close to the defect (error $>$ 0.20) however the profile of the error distribution is not affected. Error is between 2.5% and 5.0% for the region of z_c $>$ 10 mm and SC_x $<$ 15 mm.

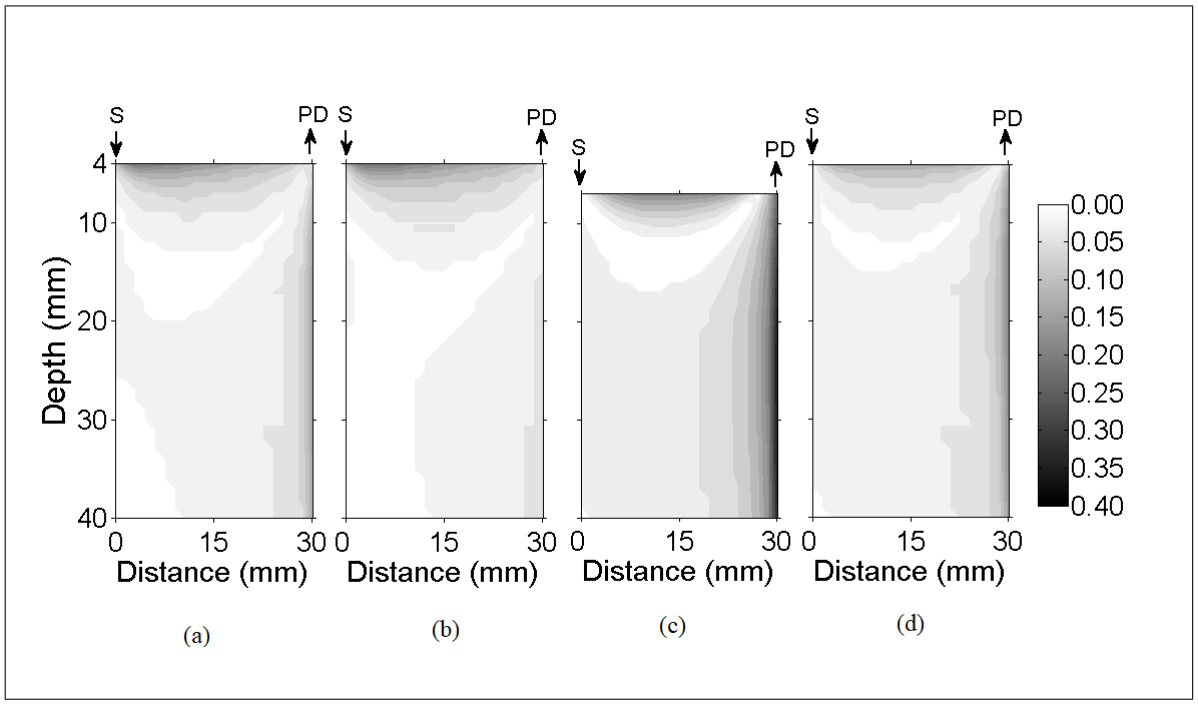

Figure 5.4 Error maps for four different situations. In general, placing the source directly above or close to the defect minimizes the error introduced by the scattering effect (error < 0.05). On the other hand, the ratio values corresponding to the superficial regions of the medium are more likely to contain a scattering effect (a-d). (b) Change in ID distorts the overlap of banana shaped SSPs of the proximal and the distal detector. Increasing ID (from 2.5 mm to 10.0 mm) does not change the error distribution when $SC_x < 25.0$ mm. (c) Defects with bigger size (5.0 mm instead of 2.0 mm) may introduce higher errors when the proximal detector is close to the defect. (d) Increase in μ_a (from 0.005 mm^{-1} to 0.050 mm^{-1}) does not change the error distribution but decreases error values. S: Source PD: Proximal Detector.

Errors in the depth estimation due to inaccuracies of lateral positioning of the defect are analyzed for the parameters in Table 5.2. For error analysis the source is assumed to be directly placed above the center of the defect however for each condition the center of the defect is thought to be dislocated up to 50% of the radius (Figure 5.5 a-d).

In general, misplacement of the source relative to the lateral position of the defect introduces an error in the depth estimation that is higher for the defects close to the surface and below 20 mm. Placing the source within 0.5mm from the center of the defect results in lower error ($< 5\%$ of the size of the defect) in depth estimation independent of inter-detector distances, size of the defect or the absorption coefficient of the medium.

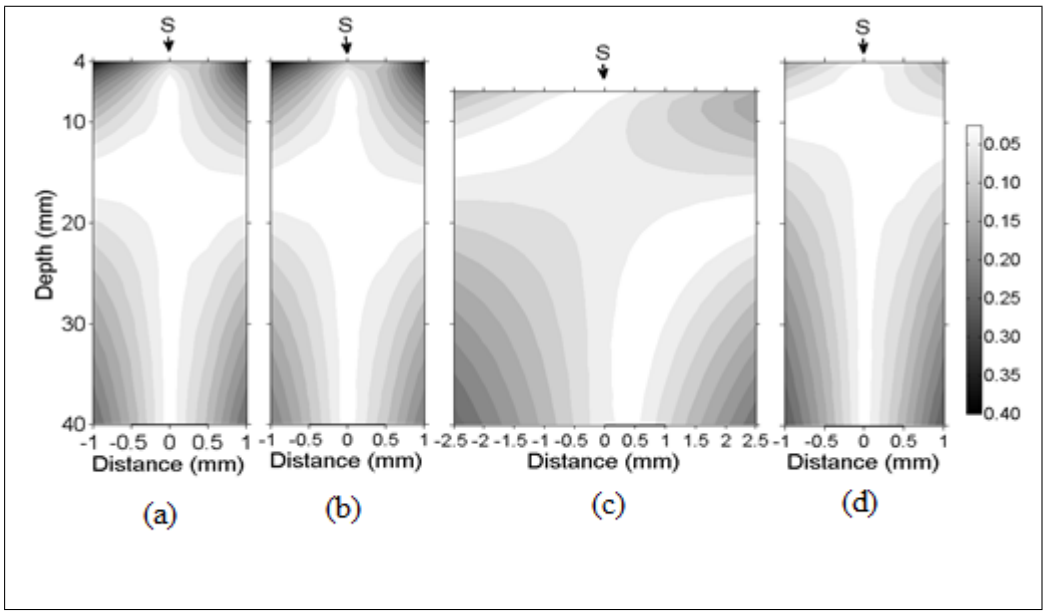

Figure 5.5 Error maps for off-center placement. Simulations are generated with the same parameters as in Table 5.2. Errors in depth estimation are below 0.10 for defects deeper than 10mm and higher than 20mm in the turbid media. The profile of error distribution is similar for different inter-detector distances (b), defects with different sizes (c) or media with different μ_a (d). S: Source.

The calculated J_0 is used to obtain the perturbation effect out of the simulated measurements (Figure 5.6) (explained in detail in Section IV.2.4.).

Results from the extended version of our method suggest that depth estimation of a defect can also be achieved using a range of optical parameters for the calculation of the background response of the probed medium. Relatively large range of optical parameters (0.005-0.060 mm^{-1} for μ_a and 0.50-3.00 mm^{-1} for μ_{st}) is chosen for the simulation that might be limited for real case applications. It should be taken into account that the actual physiologically plausible μ_a and μ_{st} are taken to reside in the selected range, which would nevertheless need good guesses to be made in advance. Another important fact is to have a finer step size (in the range of 10^{-7}; data not included) for the selected window that would allow converging to the actual optical parameters of the background medium. The necessity is to obtain multiple measurements with various distances from the source (five detectors depicted here) and employ a relatively high computational power (Figure 5.6). On the other hand, the Ratio-vs.-Depth curves that necessitate knowledge on the optical properties of the medium are not affected drastically and rough estimation (with an error up to 10%; data not included) would

be tolerated in terms of depth estimation.

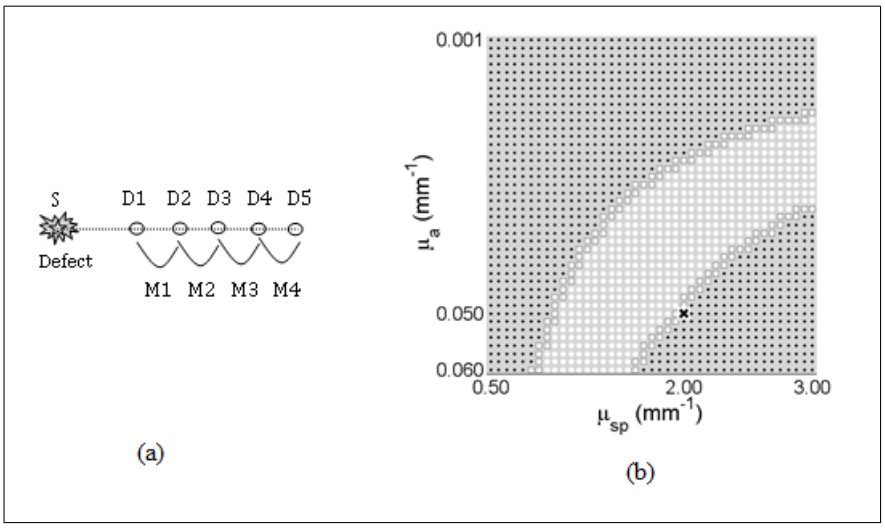

Figure 5.6 Windowing of scattering and absorption parameters of the unperturbed background response. (a) Schematic representation of the source-detector array configuration. M1-M4 the individual measurements used for depth estimation. (b) The x and y axis show the range of the absorption coefficient and reduced scattering coefficient respectively. Only the minimum-maximum and actual values are represented near axes. In this case a matrix of 42 x 41 is shown. The black and white dots are non-physical and physical results respectively. The optical parameter set selected to simulate the measured response is represented by a white square. Optical parameter set estimated from the depth values with minimum standard deviation is recognized with cross. The simulation parameters are stated in Table 2 V.1.2. Inter-detector distance is 2.5 mm for all measurements (M1-M4)

5.2 Experimental Results

The comparison of *Ratio-vs.-Depth curve* (Eq. 4.6) and experimental results is shown in Figure 35. The gray rubber cube of 1.0 cm^3 is placed in the mid-location of source-proximal detector distance (SPD) of 20.0 mm (SC_x = 10.0 mm) and inter-detector distance (ID) of 10.0 mm. The center of the defect (z_c) scanned the depth range of 15.0 mm to 40.0 mm. For this configuration, the experimental measurements of perturbed response are shown in Figure 35a in millivolts (mV). Averages of seven independent measurements as a function of depth of the defect and their corresponding standard deviations are presented. The J_0 measured by the detectors of 20.0 mm and 30.0 mm distances with respect to source are 0.291 mV and 0.075 mV respectively. The area of the detectors and the source are taken 1 mm^2 in Ratio-vs.-Depth curve generation. As expected, the measured perturbed response of proximal detector (distance of 20.0 mm) is higher than that of distal detector (Figure 5.7a).

Some of the depths assessed via experimental data and corresponding *Ratio-vs.-Depth curve* (Figure 5.6b) are shown schematically (Figure 5.6c). A cross section of the measurement geometry is shown in the figure. The light gray portion is the intralipid solution; the dark gray square shows the cross section of the cubical defect. The black dot inside the dark square is the center-of-mass of the cube, the white one is the assessed depth. Four different depths are represented, 16.0, 24.0, 32.0 and 40.0 are chosen.

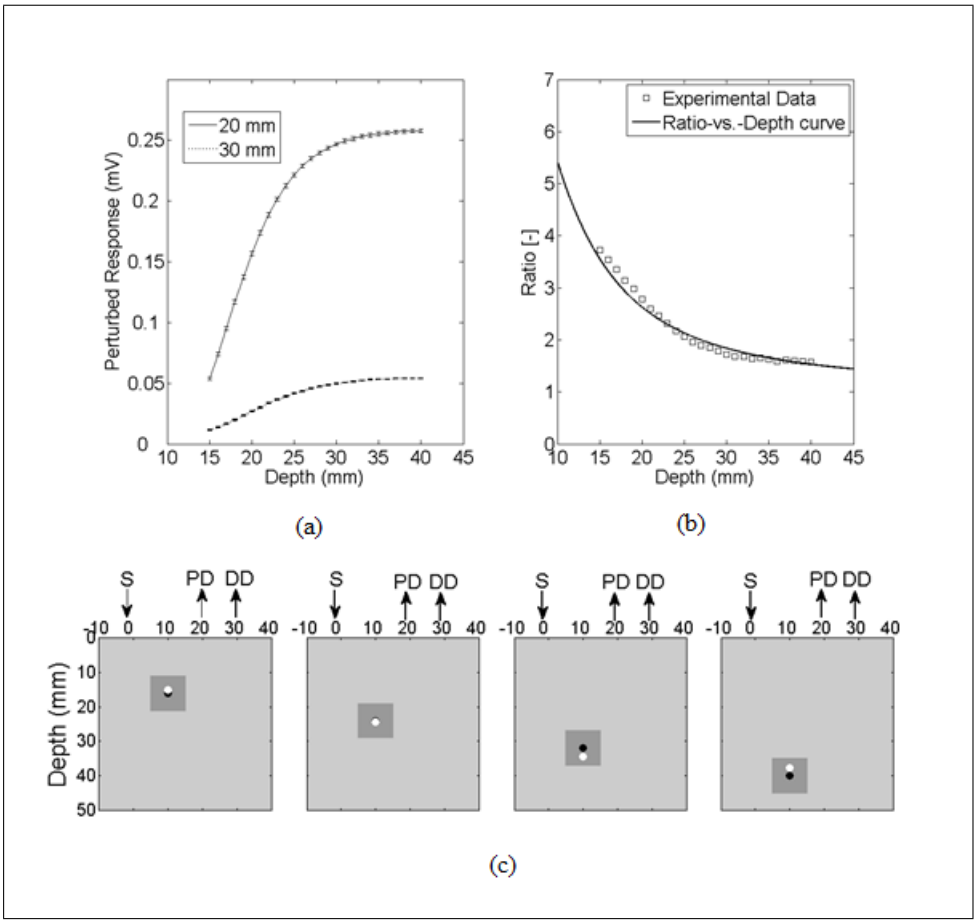

Figure 5.7 Averages and standard errors of measurement of perturbed response as a function of the depth of the center of the defect. (a) Solid and dot lines correspond to measurements of detectors at 20.0 mm and 30.0 mm distance with respect to source. Standard errors of both curves are very small with respect to average values. Experimental values are averages of seven measurements whose standard errors are shown. (b) Experimentally obtained ratio values are shown by squares and solid curve is the Ratio-vs.-Depth curve. (c) Schematic views of measurement cross section. The light gray portion depicts the aquarium filled with intralipid solution. The dark gray square is the defect (cube). Black dot inside the dark gray square shows the center-of-mass of the cube and white dot is the assessed depth. Deviations from left to right: 16.0-0.93 mm; 24.0+0.48 mm; 32.0+2.34 mm; 40.0-2.24 mm.

6. DISCUSSION

In this study a strategy to optically assess the depth of an absorber inside a semi-infinite turbid medium is proposed. The proposed method involves the use of a single CW source and an array of detectors placed in a row at different distances. By this arrangement a spatially resolved diffuse reflectance is used to obtain the perturbations introduced into the measurements by the defect. The ratio of these perturbations is then checked for the corresponding depth from the Ratio-vs.-Depth curve theoretically constructed with the same optical and spatial parameters. The proposed method does not necessitate knowledge about the size or the absorption coefficient of the defect. Several groups proposed the use of a priori information obtained from other independent imaging modalities, e.g. MRI, CT or US [18] [19] [121] [136–140]. Namely, use of a priori spatial information about the size and the location of the defect enables definition of a region-of-interest (ROI). The volume to be re-constructed could be constrained and the number of mesh-grid elements could be reduced easing the under-determinacy of the inverse problem [17]. Furthermore, use of different size mesh-grids, e.g. finer where the defect resides and coarser at other locations enables both a decrement in the under-determinacy and an increase in image resolution [30–32]. Other examples on the benefits of the use of a priori spatial information can be: use of different frequencies in frequency domain DOT imaging depending on the location of the defect to increase the imaging resolution [29], defining depth corrected reconstruction schemes [27], using variant regularization parameters [28] and variant mesh-grid sizes in assessment of physiological parameters by exogenous agents [121], using ROI to decrease the number of iterations necessary (hence time) to decrease the under-determinacy in image reconstruction [17] [34].

Ratio-vs.-Depth curves are generated by feeding the optical parameters which can be assessed by either referring to tables [5] or by experimental means [123–126] [128] [129] [141] and planar coordinates attained by SRCW diffuse reflectance measurements [42] [127] [135] into Eq. 6. Both experimentally and simulation-wise, the relative

placement of the detectors leads to a lower detection at the distal site compared to the proximal one that results in a one-to-one Ratio-vs.-Depth curves approaching 1 asymptotically. The desired knowledge on the optical properties of the medium could be a limiting factor for in vivo applications [142] [143]. To minimize this error the unperturbed response of the medium could be obtained experimentally by probing an optically similar region that is expected not to comprise a defect. Additional control schemes are suggested for cases where the optical properties of the background medium are suspected to vary from the look up tables. Our simulations presume that when the calculations for the background response are performed with a range of values around the predicted optical parameters it is possible to extract the depth of the defect from multiple measurements with an array of detectors.

Notably, the different placements of the source and detectors relative to the planar location of the defect result in curves with different characteristics (e.g. steepness). Eventually changing the arrangement of the detector pair would allow multiple checks for the depth of the defect, enabling gathering of independent values to average for more precise depth estimation. Although the simulations are conducted for a single source-double detector arrangement, the use of detector arrays can increase the precision of the method.

It should be kept in mind that the big defects might influence the error distribution. Generally, the method provides depth estimation with less than 2.5% of the size of the defect (around 0.1 mm precision) for the defects that are deeper than 10 mm from the surface of the medium. This low error is kept independent of the size of the defect (Fig 5.4c), the absorption coefficient of the defect or of the medium (Figure 5.4) as long as the source is placed close to the defect (within 0.5mm; Figure 5.5).

In the experiment, a dark gray cubical rubber is embedded in intralipid solution to simulate a defect in a semi-infinite turbid medium. It was reported by Feng et.al. [122] that the formulations developed for a spherical defect can be used safely for other kind of geometries. Due to low sensitivity of the instruments at our facility, the intralipid solution had to be diluted resulting in a relatively low absorption coefficient.

The simulations on the other hand are performed under more realistic conditions, chosen to resemble the optical properties of biological tissues [5]. The error analysis also predicts that better results can be obtained in media with higher absorption coefficient compared to the one used for the experiment (Figure 5.4d).

Even though it is not reported in detail, when the absorption coefficient of the defect with respect to medium is increased to 12-fold instead of 4-fold, the error distribution is similar to those given in this study (Figure 5.4). Therefore, the use of a dye can safely be employed to increase the contrast up to 2 or 3-fold.

The experiment to test the proposed method is conducted in an intralipid solution that mimics homogeneous turbid media, which might not be usually the case for biological specimens. However, it can be speculated that the physical principles behind the proposed method should be met when the medium has a degree of heterogeneity and the background unperturbed response is obtained experimentally and/or validated computationally with iterative methods. For example, the background response of a layered medium can be measured or calculated assuming its optical properties are characterized by a single pair of absorption and reduced scattering coefficients. However, accuracy and limitations of this approach are not studied in this work.

The present method is proposed for a single defect however more than one defect could possibly reside in a close proximity in case of biological tissues. When two defects do not coincide vertically, placing the source above one and avoiding the second to reside between source and detectors might allow to assume the second defect as a part of the unperturbed response. Additionally, by use of a forward solver of a diffusion equation for two defects, Ratio-vs.-Depth surfaces (2D version of Ratio-vs.-Depth curves) can be generated to convert the calculated ratio of perturbations into a depth value. On the other hand, for vertically aligned multiple defects the proposed method might be used to assess the average depth but not individual ones. Nevertheless, the applicability of the method for multiple defects should further be sought.

7. CONCLUSIONS

In this study a CW approach for the localization of an absorber embedded in an otherwise semi-infinite turbid media has been proposed. The motivation behind the study was to develop a method for determination of the depth of the defect independent of the size and absorption coefficient of the defect as much as possible. The method developed here works for semi-infinite geometry, which is a general case in in vivo applications. The main contribution of the study is the determination of the depth of the defect with high accuracy (0.1 mm) by using SRCW diffuse reflectance of a single wavelength without iterations when lateral position and background optical properties are predicted. Our method depends on well-known and commonly implemented physical principles [122] and mathematical derivations. It can be implemented with a NIR device (SRCW, FD or TD) without any co-registration process. Authors believe that the achieved results could be incorporated in DOI as stated in the introduction.

8. List of publications produced from the thesis

1. Localization of an absorber in a turbid semi-infinite medium by spatially resolved continuous diffuse reflectance measurements, E. B. Aksel, A. N. Türkoğlu, A. E. Ercan, A. Akın,*Journal of Biomedical Optics, SPIE*, Vol. 16, 2011.

REFERENCES

1. Fantini, S., "Optical Mammography," pp. 1–7, 2001.

2. Fantini, S., S. A. Walker, M. A. Franceschini, M. Kaschke, P. M. Schlag, and K. T. Moesta, "Assessment of the size, position, and optical properties of breast tumors in vivo by noninvasive optical methods," *Applied Optics*, Vol. 37, no. 10, p. 1982, 1998.

3. Jobsis, F. F., "Noninvasive, infrared monitoring of cerebral and myocardial oxygen sufficiency and circulatory parameters.," *Science*, Vol. 198, no. 4323, pp. 1264–1267, 1977.

4. Arridge, and J. Hebden, "Optical imaging in medicine .2. Modelling and reconstruction," *Physics in Medicine and Biology*, Vol. 42, pp. 841–853, 1997.

5. Tuchin, V. V., *Tissue optics: light scattering methods and instruments for medical diagnosis*, 2007.

6. Ishimaru, a., *Wave Propagation and Scattering in Random Media*, Vol. 8, 1978.

7. Arridge, S. R., and M. Schweiger, "Image reconstruction in optical tomography.," *Philosophical transactions of the Royal Society of London. Series B, Biological sciences*, Vol. 352, no. 1354, pp. 717–726, 1997.

8. Yodh, A., and B. Chance, "Spectroscopy and Imaging with Diffusing Light," *Physics Today*, Vol. 48, no. 3, pp. 34–40, 1995.

9. Villringer, A., and B. Chance, "Non-invasive optical spectroscopy and imaging of human brain function.," *Trends Neurosci*, Vol. 20, no. 10, pp. 435–442, 1997.

10. Brooksby, B., S. Srinivasan, S. Jiang, H. Dehghani, B. W. Pogue, K. D. Paulsen, J. Weaver, C. Kogel, and S. P. Poplack, "Spectral priors improve near-infrared diffuse tomography more than spatial priors," *Optics Letters*, Vol. 30, no. 15, p. 1968, 2005.

11. Srinivasan, S., B. W. Pogue, S. Jiang, H. Dehghani, and K. D. Paulsen, "Spectrally constrained chromophore and scattering near-infrared tomography provides quantitative and robust reconstruction," *Applied Optics*, Vol. 44, no. 10, p. 1858, 2005.

12. Li, A., Q. Zhang, J. P. Culver, E. L. Miller, and D. a. Boas, "Reconstructing chromosphere concentration images directly by continuous-wave diffuse optical tomography.," *Optics letters*, Vol. 29, no. 3, pp. 256–258, 2004.

13. Corlu, A., T. Durduran, R. Choe, M. Schweiger, E. M. C. Hillman, S. R. Arridge, and A. G. Yodh, "Uniqueness and wavelength optimization in continuous-wave multispectral diffuse optical tomography," *Optics Letters*, Vol. 28, no. 23, p. 2339, 2003.

14. Gibson, A. P., J. C. Hebden, and S. R. Arridge, "Recent advances in diffuse optical imaging," *Physics in Medicine and Biology*, Vol. 50, no. 4, pp. 1–43, 2005.

15. Schweiger, M., I. Nissilä, D. a. Boas, and S. R. Arridge, "Image reconstruction in optical tomography in the presence of coupling errors.," *Applied Optics*, Vol. 46, no. 14, pp. 2743–2756, 2007.

16. Walker, S. a., S. Fantini, and E. Gratton, "Image reconstruction by backprojection from frequency-domain optical measurements in highly scattering media.," *Applied Optics*, Vol. 36, no. 1, pp. 170–174, 1997.

17. Bai, J., T. Gao, K. Ying, and N. Chen, "Locating inhomogeneities in tissue by using the most probable diffuse path of light.," *Journal of Biomedical Optics*, Vol. 10, no. 2, p. 024024, 2005.

18. Kanmani, B., and R. M. Vasu, "Diffuse optical tomography using intensity measurements and the a priori acquired regions of interest: Theory and simulations," *Physics in Medicine and Biology*, Vol. 50, no. 2, pp. 247–264, 2005.

19. Chang, J., H. L. Graber, P. C. Koo, R. Aronson, S. L. Barbour, and R. L. Barbour, "Optical imaging of anatomical maps derived from magnetic resonance images using time-independent optical sources.," *IEEE transactions on medical imaging*, Vol. 16, no. 1, pp. 68–77, 1997.

20. Boas, D. a., M. a. O'Leary, B. Chance, and a. G. Yodh, "Detection and characterization of optical inhomogeneities with diffuse photon density waves: a signal-to-noise analysis.," *Applied Optics*, Vol. 36, no. 1, pp. 75–92, 1997.

21. den Outer, P. N., A. Lagendijk, and T. M. Nieuwenhuizen, "Location of objects in multiple-scattering media," *Journal of the Optical Society of America A*, Vol. 10, no. 6, p. 1209, 1993.

22. Matson, C. L., N. Clark, L. McMackin, and J. S. Fender, "Three-dimensional tumor localization in thick tissue with the use of diffuse photon-density waves.," *Applied optics*, Vol. 36, no. 1, pp. 214–220, 1997.

23. Gandjbakhche, A. H., R. F. Bonner, R. Nossal, and G. H. Weiss, "Absorptivity contrast in transillumination imaging of tissue abnormalities.," *Applied Optics*, Vol. 35, no. 10, pp. 1767–74, 1996.

24. Knüttel, a., J. M. Schmitt, and J. R. Knutson, "Spatial localization of absorbing bodies by interfering diffusive photon-density waves.," *Applied Optics*, Vol. 32, no. 4, pp. 381–9, 1993.

25. Wan, S. K., Z. Guo, S. Kumar, J. Aber, and B. A. Garetz, "Noninvasive detection of inhomogeneities in turbid media with time-resolved log-slope analysis," *Journal of Quantitative Spectroscopy and Radiative Transfer*, Vol. 84, no. 4, pp. 493–500, 2004.

26. Hemelt, M. W., and K. A. Kang, "Determination of a biological absorber depth utilizing multiple source-detector separations and multiple frequency values of near-infrared time-resolved spectroscopy," *Biotechnology Progress*, Vol. 15, no. 4, pp. 622–629, 1999.

27. Huang, M., and Q. Zhu, "Dual-Mesh Optical Tomography Reconstruction Method with a Depth Correction that Uses A Priori Ultrasound Information," *Applied Optics*, Vol. 43, no. 8, pp. 1654–1662, 2004.

28. Pogue, B. W., T. O. Mcbride, J. Prewitt, U. L. Österberg, and K. D. Paulsen, "Spatially variant regularization improves diffuse optical tomography," *Applied Optics*, Vol. 38, no. 13, p. 2950, 1999.

29. Zhu, Q., C. Xu, P. Guo, and A. Aguirre, "Optimal probing of optical contrast of breast lesions of different size located at different depths by US localization," *Technology in cancer research & treatment*, Vol. 5, no. 4, pp. 365–380, 2006.

30. Dehghani, H., B. W. Pogue, S. D. Jiang, B. Brooksby, and K. D. Paulsen, "Three-dimensional optical tomography: resolution in small-object imaging," *Applied Optics*, Vol. 42, no. 16, pp. 3117–3128, 2003.

31. Guven, M., B. Yazici, K. Kwon, E. Giladi, and X. Intes, "Effect of discretization error and adaptive mesh generation in diffuse optical absorption imaging: II," *Inverse Problems*, Vol. 23, no. 3, pp. 1135–1160, 2007.

32. Guven, M., B. Yazici, X. Intes, and B. Chance, "An adaptive multigrid algorithm for region of interest diffuse optical tomography," in *IEEE International Conference on Image Processing*, Vol. 2, pp. 823–826, 2003.

33. Lin, Y., H. Gao, O. Nalcioglu, and G. Gulsen, "Fluorescence diffuse optical tomography with functional and anatomical a priori information: Feasibility study," *Physics in Medicine and Biology*, Vol. 52, no. 18, pp. 5569–5585, 2007.

34. Zhu, Q., N. Chen, and S. H. Kurtzman, "Imaging tumor angiogenesis by use of combined near-infrared diffusive light and ultrasound.," *Optics Letters*, Vol. 28, no. 5, pp. 337–339, 2003.

35. Zhu, Q., M. Huang, N. Chen, K. Zarfos, B. Jagjivan, M. Kane, P. Hedge, and S. H. Kurtzman, "Ultrasound-guided optical tomographic imaging of malignant and benign breast lesions: initial clinical results of 19 cases," *Neoplasia*, Vol. 5, no. 5, pp. 379–388, 2003.

36. Weatherall, P., G. F. Evans, G. J. Metzger, M. H. Saborrian, and A. M. Leitch, "MRI vs. histologic measurement of breast cancer following chemotherapy: comparison with x-ray mammography and palpation," *Journal of Magnetic Resonance Imaging*, Vol. 13, pp. 868–875, 2001.

37. Li, A., J. Liu, W. Tanamai, R. Kwong, A. E. Cerussi, and B. J. Tromberg, "Assessing the spatial extent of breast tumor intrinsic optical contrast using ultrasound and diffuse optical spectroscopy.," *Journal of Biomedical Optics*, Vol. 13, no. 3, p. 030504, 2009.

38. Bohren, C. F., and D. R. Huffman, *Absorption and Scattering of Light by Small Particles*, Vol. 1, 1998.

39. Halliday, and Resnick, *Fundamental of Physics 10th Edition*, Vol. 1, 2015.

40. Griffiths, D. J., and C. Inglefield, *Introduction to Electrodynamics*, Vol. 73, 2005.

41. Feynman, R. P., Leighton, Sands, R. B. Leighton, and M. Sands, "The Feynman Lectures on Physics," *Feynmanlectures.Caltech.Edu*, Vol. 33, no. 9, p. 750, 1965.

42. Gratton, G., J. S. Maier, M. Fabiani, W. W. Mantulin, and E. Gratton, "Feasibility of intracranial near-infrared optical scanning," in *Psychophysiology*, Vol. 31, pp. 211–215, 1994.

43. Matcher, S. J., "Nonuniqueness in optical tomography: relevance of the P1 approximation.," *Optics Letters*, Vol. 24, no. 23, pp. 1729–31, 1999.

44. Reynolds, L., C. Johnson, and A. Ishimaru, "Diffuse reflectance from a finite blood medium: applications to the modeling of fiber optic catheters," *Applied Optics*, Vol. 15, no. 9, p. 2059, 1976.

45. Kienle, A., "Anisotropic light diffusion: An oxymoron?," *Physical Review Letters*, Vol. 98, no. 21, pp. 1–4, 2007.

46. Binzoni, T., T. S. Leung, a. H. Gandjbakhche, G. RÃÂ$\frac{1}{4}$fenacht, D. T. Delpy, and D. Rüfenacht, "The use of the Henvey-Greenstein phase function in {Monte Carlo} simulations in biomedical optics," *Physics In Medicine And Biology*, Vol. 51, no. 17, pp. N313–N322, 2006.

47. Dagdug, L., G. H. Weiss, and A. H. Gandjbakhche, "Effects of anisotropic optical properties on photon migration in structures tissues," *Physics In Medicine And Biology*, Vol. 48, pp. 1361–1370, 2003.

48. Nickell, S., M. Hermann, M. Essenpreis, T. J. Farrell, U. Kr, and M. S. Patterson, "Anisotropy of light propagation in human skin," *Physics In Medicine And Biology*, Vol. 45, pp. 2873–2886, 2000.

49. Flock, S. T., B. C. Wilson, and M. S. Patterson, "Total attenuation coefficients and scattering phase functions of tissues and phantom materials at 633 nm," *Medical Physics*, Vol. 14, no. 5, pp. 835–841, 1987.

50. van der Zee, P., and D. T. Delpy, "Computed point spread functions for light in tissue using a measured volume scattering function.," *Adv Exp Med Biol.*, Vol. 222, pp. 191–197, 1988.

51. Cheong, W.-F., S. A. Prahl, and A. J. Welch, "A Review of the Optical Properties of Biological Tissues," *IEEE Journal of Quantum Electronics*, Vol. 26, no. 12, pp. 2166–2185, 1990.

52. Arnfield, M. R., J. Tulip, and M. S. Mcphee, "Optical propagation in tissue with anisotropic scattering," *IEEE Transactions on Biomedical Engineering*, Vol. 35, no. 5, pp. 372–381, 1988.

53. Graaff, R., J. G. Aarnoudse, F. F. de Mul, and H. W. Jentink, "Light propagation parameters for anisotropically scattering media based on a rigorous solution of the transport equation.," *Applied Optics*, Vol. 28, no. 12, pp. 2273–2279, 1989.

54. Liu, P. Y., "A New Phase Function Approximating to Mie Scattering for Radiative Transport-Equations," *Physics In Medicine And Biology*, Vol. 39, no. 6, pp. 1025–1036, 1994.

55. Wang, L. V., and S. L. Jacques, "Source of error in calculation of optical diffuse reflectance from turbid media using diffusion theory," *Computer Methods and Programs in Biomedicine*, Vol. 61, no. 3, pp. 163–170, 2000.

56. Wang, L., S. L. Jacques, and L. Zheng, "MCML-Monte Carlo modeling of light transport in multi-layered tissues," *Computer Methods and Programs in Biomedicine*, Vol. 47, no. 2, pp. 131–146, 1995.

57. Jacques, S. L., C. A. Alter, and S. Prahl, "Angular dependence of HeNe laser light scattering by human dermis," *Lasers in the Life Sciences*, Vol. 1, pp. 309–333, 1987.

58. Binzoni, T., T. S. Leung, A. H. Gandjbakhche, D. Rüfenacht, and D. T. Delpy, "Comment on 'The use of the Henyey-Greenstein phase function in Monte Carlo simulations in biomedical optics'," *Physics in Medicine and Biology*, Vol. 51, no. 22, pp. 39–41, 2006.

59. Canpolat, M., and J. R. Mourant, "High-angle scattering events strongly affect light collection in clinically relevant measurement geometries for light transport through tissue," *Physics in Medicine and Biology*, Vol. 45, no. 5, pp. 1127–1140, 2000.

60. Ishimaru, A., "Diffusion of light in turbid material.," *Applied Optics*, Vol. 28, no. 12, pp. 2210–5, 1989.

61. Johnson, C. C., "Optical Diffusion in Blood," *IEEE Transactions on Biomedical Engineering*, Vol. BME-17, no. 2, pp. 129–133, 1970.

62. Barer, R., "Spectrophotometry of clarified cell suspensions.," *Science*, Vol. 121, no. 3151, pp. 709–715, 1955.

63. Okada, E., and D. T. Delpy, "Near-infrared light propagation in an adult head model I Modeling of low-level scattering in the cerebrospinal fluid layer," *Applied Optics*, Vol. 42, no. 16, p. 2906, 2003.

64. Okada, E., and D. T. Delpy, "Near-infrared light propagation in an adult head model II Effect of superficial tissue thickness on the sensitivity of the near-infrared spectroscopy signal," *Applied Optics*, Vol. 42, no. 16, p. 2915, 2003.

65. Okada, E., M. Firbank, and D. T. Delpy, "The effect of ovelying tissue on the spatial sensitivity profine on near-infrared spectroscopy," *Physics in Medicine and Biology*, Vol. 40, no. 40, pp. 2093–2108, 1995.

66. Ishimaru, A., "Diffusion of a pulse in densely distributed scatterers," *Journal of the Optical Society of America*, Vol. 68, no. 8, p. 1045, 1978.

67. Huang, Y., X. G. Liang, and X. L. Xia, "Monte Carlo simulation of radiative transfer in scattering, emitting, absorbing slab with gradient index," *Journal of Quantitative Spectroscopy and Radiative Transfer*, Vol. 92, no. 1, pp. 111–120, 2005.

68. Huang, K., "Statistical Mechanics, 2nd Edition," 1987.

69. Arridge, S. R., "Optical tomography in medical imaging," *Inverse Problems*, Vol. 15, no. 2, pp. R41–R93, 1999.

70. Boas, D. a., K. Chen, D. Grebert, and M. A. Franceschini, "Improving the diffuse optical imaging spatial resolution of the cerebral hemodynamic response to brain activation in humans.," *Optics Letters*, Vol. 29, no. 13, pp. 1506–1508, 2004.

71. Boas, D. A., and A. M. Dale, "Simulation study of magnetic resonance imaging-guided cortically constrained diffuse optical tomography of human brain function," *Applied Optics*, Vol. 44, no. 10, p. 1957, 2005.

72. Boas, D. A., G. Strangman, J. P. Culver, R. Hoge, G. Jasdzewski, R. A. Poldrack, B. R. Rosen, and J. B. Mandeville, "Can the cerebral metabolic rate of oxygen be estimated with near-infrared spectroscopy ?," *Physics in Medicine and Biology*, Vol. 48, pp. 2405–2418, 2003.

73. Boas, D. A., T. Gaudette, G. Strangman, X. Cheng, J. J. Marota, and J. B. Mandeville, "The accuracy of near infrared spectroscopy and imaging during focal changes in cerebral hemodynamics," *NeuroImage*, Vol. 13, no. 1, pp. 76–90, 2001.

74. Boas, D. A., M. A. Oleary, B. Chance, and A. G. Yodh, "Scattering of Diffuse Photon Density Waves by Spherical Inhomogeneities Within Turbid Media - Analytic Solution and Applications," *Proceedings of the National Academy of Sciences of the United States of America*, Vol. 91, no. 11, pp. 4887–4891, 1994.

75. Boas, D. A., M. A. O'Leary, B. Chance, and A. G. Yodh, "Scattering and wavelength transduction of diffuse photon density waves," *Physical Review E*, Vol. 47, no. 5, 1993.

76. Weinberg, A., and E. Wigner, *Physical Theory of Neutron Chain Reactors.*, University of Chicago Press, first edit ed., 1958.

77. Yoo, K. M., F. Liu, and R. R. Alfano, "When does the diffusion approximation fail to describe photon transport in random media?," *Physical Review Letters*, Vol. 64, no. 22, pp. 2647–2650, 1990.

78. Morse, P. M., *Methods of Theoretical Physics*, Vol. 22, 1954.

79. Tsuchiya, Y., and T. Urakami, "Quantitation of absorbing substances in turbid media such as human tissues based on the microscopic Beer-Lambert law," *Optics communications*, Vol. 144, no. December, pp. 269–280, 1997.

80. Colasanti, A., G. Guida, A. Kisslinger, R. Liuzzi, M. Quarto, P. Riccio, G. Roberti, and F. Villani, "Multiple processor version of a Monte Carlo code for photon transport in turbid media," *Computer Physics Communications*, Vol. 132, no. 1-2, pp. 84–93, 2000.

81. Hiraoka, M., M. Firbank, M. Essenpreis, M. Cope, S. R. Arridge, P. Van Der Zee, and D. T. Delpy, "A Monte Carlo investigation of optical pathlength in inhomogeneous tissue and its application to near-infrared spectroscopy," *Physics in Medicine and Biology*, Vol. 38, no. 12, pp. 1859–1876, 1993.

82. Kurth, C. D., Hanli Liu, W. S. Thayer, and B. Chance, "A dynamic phantom brain model for near-infrared spectroscopy," *Physics in Medicine and Biology*, Vol. 40, no. 12, pp. 2079–2092, 1995.

83. Graaff, R., M. H. Koelink, F. F. M. de Mul, W. G. Zijlstra, A. C. M. Dassel, and J. G. Aarnoudse, "Condensed Monte Carlo simulations for the description of light transport," *Applied Optics*, Vol. 32, no. 4, p. 426, 1993.

84. Kienle, a., L. Lilge, M. S. Patterson, R. Hibst, R. Steiner, and B. C. Wilson, "Spatially resolved absolute diffuse reflectance measurements for noninvasive determination of the optical scattering and absorption coefficients of biological tissue.," *Applied Optics*, Vol. 35, no. 13, pp. 2304–2314, 1996.

85. L'Ecuyer, P., "Good Parameters and Implementations for Combined Multiple Recursive Random Number Generators," *Operations Research*, Vol. 47, no. 1, pp. 159–164, 1999.

86. L'Ecuyer, P., and S. Cote, "Implementing a random number package with splitting facilities," *ACM Transactions on Mathematical Software*, Vol. 17, no. 1, pp. 98–111, 1991.

87. L'Ecuyer, P., "Random Number Generation with Multiple Streams for Sequential and Parallel Computing," *Proceedings of the 2015 Winter Simulation Conference*, no. 1991, pp. 31–44, 2015.

88. Cheng, X., and D. Boas, "Diffuse optical reflection tomography using continuous wave illumination.," *Optics Express*, Vol. 3, no. 3, pp. 118–123, 1998.

89. Li, X. D., T. Durduran, a. G. Yodh, B. Chance, and D. N. Pattanayak, "Diffraction tomography for biochemical imaging with diffuse-photon density waves.," *Optics Letters*, Vol. 22, no. 8, pp. 573–5, 1997.

90. Matson, C., "A diffraction tomographic model of the forward problem using diffuse photon density waves.," *Optics Express*, Vol. 1, no. 1, pp. 6–11, 1997.

91. Matson, C. L., and H. Liu, "Analysis of the forward problem with diffuse photon density waves in turbid media by use of a diffraction tomography model," *Journal of the Optical Society of America A*, Vol. 16, no. 3, p. 455, 1999.

92. Scholkmann, F., S. Kleiser, A. J. Metz, R. Zimmermann, J. Mata Pavia, U. Wolf, and M. Wolf, "A review on continuous wave functional near-infrared spectroscopy and imaging instrumentation and methodology," *NeuroImage*, Vol. 85, pp. 6–27, 2014.

93. Boas, D. A., D. H. Brooks, E. L. Miller, C. A. Dimarzio, M. Kilmer, R. J. Gaudette, and Q. Zhang, "Imaging the body with diffuse optical tomography," *IEEE Signal Processing Magazine*, Vol. 18, no. 6, pp. 57–75, 2001.

94. Cohen, L. B., "Changes in neuron structure during action potential propagation and synaptic transmission.," *Physiological Reviews*, Vol. 53, no. 2, pp. 373–418, 1973.

95. Chance, B., Q. Luo, S. Nioka, D. C. Alsop, and J. A. Detre, "Optical investigations of physiology: a study of intrinsic and extrinsic biomedical contrast.," *Philosophical transactions of the Royal Society of London. Series B, Biological sciences*, Vol. 352, no. 1354, pp. 707–716, 1997.

96. Rector, D. M., G. R. Poe, M. P. Kristensen, and R. M. Harper, "Light scattering changes follow evoked potentials from hippocampal Schaeffer collateral stimulation.," *Journal of Neurophysiology*, Vol. 78, no. 3, pp. 1707–1713, 1997.

97. Hill, D. K., and R. D. Keynes, "Opacity changes in stimulated nerve," *The Journal of Physiology*, Vol. 108, no. 3, pp. 278–281, 1949.

98. Medvedev, A. V., J. M. Kainerstorfer, S. V. Borisov, A. H. Gandjbakhche, and J. VanMeter, ""Seeing" electroencephalogram through the skull: imaging prefrontal cortex with fast optical signal," *Journal of Biomedical Optics*, Vol. 15, no. 6, p. 061702, 2010.

99. Wong-Riley, M. T. T., "Cytochrome oxidase: an endogenous marker for neuron activity," *Trends in Neurosciences*, Vol. 12, no. 3, pp. 94–101, 1989.

100. Cope, M., and D. T. Delpy, "System for long-term measurement of cerebral blood and tissue oxygenation on newborn infants by near infra-red transillumination," *Medical & Biological Engineering & Computing*, Vol. 26, no. 3, pp. 289–294, 1988.

101. Franceschini, M. A., and D. A. Boas, "Noninvasive measurement of neuronal activity with near-infrared optical imaging," *NeuroImage*, Vol. 21, no. 1, pp. 372–386, 2004.

102. Delpy, D. T., and M. Cope, "Quantification in tissue near-infrared spectroscopy," *Philosophical Transactions of the Royal Society B: Biological Sciences*, Vol. 352, no. 1354, pp. 649–659, 1997.

103. Ito, H., I. Kanno, H. Fukuda, H. I. To, I. K. Anno, H. F. Ukuda, H. Ito, I. Kanno, and H. Fukuda, "Human cerebral circulation : positron emission tomography studies," *Annals of Nuclear Medicine*, Vol. 19, no. 2, pp. 65–74, 2005.

104. Franceschini, M. A., S. Fantini, J. H. Thompson, J. P. Culver, and D. A. Boas, "Hemodynamic evoked response of the sensorimotor cortex measured noninvasively with near-infrared optical imaging," *Psychophysiology*, Vol. 40, no. 4, pp. 548–560, 2003.

105. Toronov, V., M. A. Franceschini, M. Filiaci, Fantini.S, M. Wolf, A. Michalos, and E. Gratton, "Near infrared study of fluctuation in cerebral hemodynamics during rest and motor stimulation: temporal analysis and spatial mapping," *Med. Phys.*, Vol. 27, pp. 801–815, 2000.

106. Steinbrink, J., M. Kohl, H. Obrig, G. Curio, F. Syre', F. Thomas, H. Wabnitz, H. Rinneberg, and A. Villringer, "Somatosensory evoked fast optical intensity changes detected non-invasively in the adult human head.," *Neurosciense Letters*, Vol. 291, no. 2, pp. 105–108, 2000.

107. Wolf, M., U. Wolf, J. H. Choi, R. Gupta, L. P. Safonova, L. A. Paunescu, A. Michalos, and E. Gratton, "Functional frequency-domain near-infrared spectroscopy detects fast neuronal signal in the motor cortex," *NeuroImage*, Vol. 17, no. 4, pp. 1868–1875, 2002.

108. Gratton, G., M. Fabiani, P. M. Corballis, D. C. Hood, M. R. Goodman-Wood, J. Hirsch, K. Kim, D. Friedman, and E. Gratton, "Fast and localized event-related optical signals(EROS) in the human occipital cortex: Comparisons with the visual evoked potential and fMRI," *NeuroImage*, Vol. 6, no. 3, pp. 168–180, 1997.

109. Wolf, M., U. Wolf, J. H. Choi, V. Toronov, L. A. Paunescu, A. Michalos, and E. Gratton, "Fast cerebral functional signal in the 100-ms range detected in the visual cortex by frequency-domain near-infrared spectrophotometry," *Psychophysiology*, Vol. 40, no. 4, pp. 521–528, 2003.

110. Maclin, E. L., K. A. Low, J. J. Sable, M. Fabiani, and G. Gratton, "The event-related optical signal to electrical stimulation of the median nerve," *NeuroImage*, Vol. 21, no. 4, pp. 1798–1804, 2004.

111. Rinne, T., G. Gratton, M. Fabiani, N. Cowan, E. Maclin, A. Stinard, J. Sinkkonen, K. Alho, and R. Näätänen, "RAPID COMMUNICATION Scalp-Recorded Optical Signals Make Sound Processing in the Auditory Cortex Visible?," *NeuroImage*, Vol. 10, no. 5, pp. 620–624, 1999.

112. Syré, F., H. Obrig, J. Steinbrink, M. Kohl, R. Wenzel, and A. Villringer, "Are VEP correlated fast optical signals detectable in the human adult by non-invasive nearinfrared spectroscopy (NIRS)?," *Adv Exp Med Biol*, Vol. 530, pp. 421–431, 2003.

113. Steinbrink, J., F. C. D. Kempf, A. Villringer, and H. Obrig, "The fast optical signal - Robust or elusive when non-invasively measured in the human adult?," *NeuroImage*, Vol. 26, no. 4, pp. 996–1008, 2005.

114. Intes, X., C. Maloux, M. Guven, B. Yazici, and B. Chance, "Diffuse optical tomography with physiological and spatial a priori constraints," *Physics in Medicine and Biology*, Vol. 49, no. 12, pp. 155–163, 2004.

115. Kim, K.-R., H.-E. Moon, and K.-W. Kim, "Hypoxia-induced angiogenesis in human hepatocellular carcinoma.," *Journal of Molecular Medicine (Berlin, Germany)*, Vol. 80, no. 11, pp. 703–14, 2002.

116. Choi, K. S., M. K. Bae, J. W. Jeong, H. E. Moon, and K. W. Kim, "Hypoxia-induced angiogenesis during carcinogenesis," *Journal of Biochemistry and Molecular Biology*, Vol. 36, no. 1, pp. 120–127, 2003.

117. Naumov, G. N., J. Folkman, O. Straume, and L. A. Akslen, "Tumor-vascular interactions and tumor dormancy," *APMIS*, Vol. 116, no. 7–8, p. 569–585, 2008.

118. Palmer, G. M., A. N. Fontanella, G. Zhang, G. Hanna, C. L. Fraser, and M. W. Dewhirst, "Optical imaging of tumor hypoxia dynamics," *Journal of Biomedical Optics*, Vol. 15, no. 6, p. 066021, 2010.

119. Leung, T. S., N. Aladangady, C. E. Elwell, D. T. Delpy, and K. Costeloe, "A New Method for the Measurement of Cerebral Blood Volume and Total Circulating Blood Volume Using Near Infrared Spatially Resolved Spectroscopy and Indocyanine Green: Application and Validation in Neonates," *Pediatric Research*, Vol. 55, no. 1, pp. 134–141, 2004.

120. Dunn, J. F., Q. Zhang, Y. Wu, S. Srinivasan, M. R. Smith, and R. A. Shaw, "Monitoring angiogenesis noninvasively with near-infrared spectroscopy.," *Journal of Biomedical Optics*, Vol. 13, no. 6, p. 064043, 2008.

121. Unlu, M. B., O. Birgul, and G. Gulsen, "A simulation study of the variability of indocyanine green kinetics and using structural a priori information in dynamic contrast enhanced diffuse optical tomography (DCE-DOT)," *Physics in Medicine and Biology*, Vol. 53, no. 12, pp. 3189–3200, 2008.

122. Feng, S., F. a. Zeng, and B. Chance, "Photon migration in the presence of a single defect: a perturbation analysis.," *Applied Optics*, Vol. 34, no. 19, pp. 3826–3837, 1995.

123. Doornbos, R. M. P., R. Lang, M. C. Aalders, F. W. Cross, and H. J. C. M. Sterenborg, "The determination of in vivo human tissue optical properties and absolute chromophore concentrations using spatially resolved steady-state diffuse reflectance spectroscopy," *Physics in Medicine and Biology*, Vol. 44, no. 4, pp. 967–981, 1999.

124. Dimofte, A., J. C. Finlay, and T. C. Zhu, "A method for determination of the absorption and scattering properties interstitially in turbid media," *Physics in Medicine and Biology*, Vol. 50, no. 10, pp. 2291–2311, 2005.

125. Liu, H., D. a. Boas, Y. Zhang, a. G. Yodh, and B. Chance, "Determination of optical properties and blood oxygenation in tissue using continuous NIR light.," *Physics in Medicine and Biology*, Vol. 40, no. 11, pp. 1983–1993, 1995.

126. Patterson, M. S., B. Chance, and B. C. Wilson, "Time resolved reflectance and transmittance for the noninvasive measurement of tissue optical properties," *Applied Optics*, Vol. 28, no. 12, p. 2331, 1989.

127. Akatsuki, A. T., H. E. Da, T. Y. Anagida, and A. S. Eiyama, "Absorber ' s Effect Projected Directly Above Improves Spatial Resolution in Near Infrared Backscattered Imaging," *Japanese Journal of Physiology*, Vol. 54, no. 1, pp. 79–86, 2004.

128. Kienle, A., and M. S. Patterson, "Determination of the optical properties of semi-infinite turbid media from frequency-domain reflectance close to the source," *Physics in Medicine and Biology*, Vol. 42, no. 9, pp. 1801–1819, 1997.

129. Kienle, A., and M. S. Patterson, "Determination of the optical properties of turbid media from a single Monte Carlo simulation.," *Physics in Medicine and Biology*, Vol. 41, no. 10, pp. 2221–2227, 1996.

130. Kumar, G., and J. M. Schmitt, "Optimal probe geometry for near-infrared spectroscopy of biological tissue.," *Applied Optics*, Vol. 36, no. 10, pp. 2286–2293, 1997.

131. Martelli, F., A. Sassaroli, G. Zaccanti, and Y. Yamada, "Properties of the light emerging from a diffusive medium: Angular dependence and flux at the external boundary," *Physics in Medicine and Biology*, Vol. 44, no. 5, pp. 1257–1275, 1999.

132. Farrell, T. J., M. S. Patterson, and B. Wilson, "A diffusion theory model of spatially resolved, steady-state diffuse reflectance for the noninvasive determination of tissue optical properties in vivo.," *Medical Physics*, Vol. 19, no. 4, pp. 879–888, 1992.

133. Cui, W., C. Kumar, and B. Chance, "Experimental study of migration depth for the photons measured at sample surface," *Proc. SPIE*, Vol. 1431, pp. 180–191, 1991.

134. Weiss, G. H., R. Nossal, and R. F. Bonner, "Statistics of penetration depth of photons re-emitted from irradiated tissue," *Journal of Modern Optics*, Vol. 36, no. 3, pp. 349–359, 1989.

135. Sassaroli, A., C. Blumetti, F. Martelli, L. Alianelli, D. Contini, A. Ismaelli, and G. Zaccanti, "Monte Carlo procedure for investigating light propagation and imaging of highly scattering media.," *Applied Optics*, Vol. 37, no. 31, pp. 7392–7400, 1998.

136. Barbour, L., L. Graber, and P. C. Koo, "MRLGuided Optical Tomography : Prospects and Computation for a New ' Imaging Method," 1995.

137. Schweiger, M., and S. R. Arridge, "Application of temporal filters to time resolved data in optical tomography," *Physics in Medicine and Biology*, Vol. 1699, pp. 1699–1717, 1999.

138. Li, A., E. L. Miller, M. E. Kilmer, T. J. Brukilacchio, T. Chaves, J. Stott, Q. Zhang, T. Wu, M. Chorlton, R. H. Moore, D. B. Kopans, and D. A. Boas, "Tomographic optical breast imaging guided by three-dimensional mammography," *Applied Optics*, Vol. 42, no. 25, p. 5181, 2003.

139. Boverman, G., E. L. Miller, A. Li, Q. Zhang, T. Chaves, D. H. Brooks, and D. A. Boas, "Quantitative spectroscopic diffuse optical tomography of the breast guided by imperfect a priori structural information," *Physics in Medicine and Biology*, Vol. 50, no. 17, pp. 3941–3956, 2005.

140. Brooksby, B. A., H. Dehghani, B. W. Poque, and K. D. Paulsen, "Near-infrared (NIR) tomography breast image reconstruction with a priori structural information from MRI: Algorithm development for reconstructing heterogeneities," *IEEE Journal on Selected Topics in Quantum Electronics*, Vol. 9, no. 2, pp. 199–209, 2003.

141. Farrell, T. J., B. C. Wilson, and M. S. Patterson, "The use of a neural network to determine tissue optical properties from spatially resolved diffuse reflectance measurements," *Physics in Medicine and Biology*, Vol. 37, no. 12, pp. 2281–2286, 1992.

142. Okada, E., M. Firbank, M. Schweiger, S. R. Arridge, M. Cope, and D. T. Delpy, "Theoretical and experimental investigation of near-infrared light propagation in a model of the adult head.," *Applied Optics*, Vol. 36, no. 1, pp. 21–31, 1997.

143. Carbone, N., H. Di Rocco, D. I. Iriarte, and J. a. Pomarico, "Solution of the direct problem in turbid media with inclusions using Monte Carlo simulations implemented in graphics processing units: new criterion for processing transmittance data.," *Journal of Biomedical Optics*, Vol. 15, no. 3, p. 035002, 2014.